

Variations in global zonal wind from 18 to 100 km due to solar activity, and QBO, ENSO during 2002–2019

Xiao Liu^{1,2}, Jiyao Xu^{2,3}, Jia Yue^{4,5}, and Vania F. Andrioli^{2,6}

¹Institute of Electromagnetic Wave, School of Physics, Henan Normal University, Xinxiang, 453000, China

²State Key Laboratory of Space Weather, National Space Science Center, Chinese Academy of Sciences, Beijing, 100190, China

³University of the Chinese Academy of Science, Beijing, 100049, China

⁴Physics Department, Catholic University of America, Washington, DC 20064, USA

⁵NASA Goddard Space Flight Center, Greenbelt, MD, 20771, USA

⁶Heliophysics, Planetary Science and Aeronomy Division, National Institute for Space Research (INPE), Sao Jose dos Campos, Sao Paulo, Brazil

Correspondence to: Jiyao Xu (xujy@nssc.ac.cn)

Key Points:

- The seasonal and linear variations of zonal winds coincide with those of MERRA2 with slight differences in magnitudes.
- The responses of zonal winds to QBO are approximately hemispheric symmetry and change from positive to negative with the increasing height.
- The responses of zonal winds to F10.7 and ENSO are more prominent in the southern stratospheric polar jet region as compared to that the northern counterpart.

23 Abstract

24 Variations of global wind are important in changing the atmospheric structure and circulation, in coupling of
25 atmospheric layers, in influencing the wave propagations. Due to the difficulty of directly measuring zonal wind from the
26 stratosphere to the lower thermosphere, we derived a global balance wind (BU) dataset from 50°S to 50°N and during 2002–
27 2019 using the gradient wind theory and SABER temperatures and modified by meteor radar observations at the equator.
28 The dataset captures the main feature of global monthly mean zonal wind and can be used to study the variations (i.e., annual,
29 semi-annual, ter-annual, and linear) of zonal wind and the responses of zonal wind to QBO (quasi-biennial oscillation),
30 ENSO (El Niño/Southern Oscillation), and solar activity. Same procedure is performed on the MERRA2 zonal wind (MerU)
31 to validate BU and its responses below 70 km. The annual, semi-annual, ter-annual oscillations of BU and MerU have
32 similar amplitudes and phases. The semi-annual oscillation of BU has peaks around 80 km, which are stronger in the
33 southern tropical region and coincide with previous satellite observations. As the increasing of the QBO wind, both BU and
34 MerU change from increasing to decreasing with the increasing height and extend from the equator to higher latitudes. Both
35 BU and MerU increase with the increasing of MEI (an indicator of ENSO) and decrease with increasing F10.7 (an indicator
36 of solar activity) in the southern stratospheric polar jet region below 70 km. The responses of winds to ENSO and F10.7
37 exhibit hemispheric asymmetry and are more significant in the southern polar jet region. While above 70 km, BU increases
38 with the increasing of MEI and F10.7. The negative linear changes of BU at 50°N are absent in MerU during October–
39 January. The discussions on the possible influences of the temporal intervals and sudden stratospheric warmings (SSWs) on
40 the variations and responses of BU illustrate that: (1) the seasonal variations and the responses to QBO are almost
41 independent on the temporal intervals selected; (2) the responses to ENSO and F10.7 are robust but slightly depend on the
42 temporal intervals; (3) the linear changes of both BU and MerU depend strongly on the temporal intervals; (4) SSWs affect
43 the magnitudes but do not affect the hemispheric asymmetry of the variations and responses of BU at least in the monthly
44 mean sense. The variations and responses of global zonal wind to various factors are based on BU, which is derived from
45 observations, and thus provide a good complementary to model studies and ground-based observations.

46 1 Introduction

47 Atmospheric dynamics field (temperature, wind, etc.) and species not only exhibit latitude, longitude, and height
48 variations, but also exhibit temporal variations with periods ranging from days, months to years, and even decade. The
49 temporal variations can be ascribed into long-term variations, intra-annual and inter-annual variations. Here the long-term
50 variations mean the linear term or linear change in a regression model and on a time scale longer than one solar cycle in the
51 middle and upper atmosphere. The long-term variations of the middle and upper atmosphere have been received attentions
52 due to the greenhouse gases driven anthropogenic climate change and its influences on atmospheric drag and thus our space
53 vehicles (Beig et al., 2003, 2008; Laštovička, 2017; Yue et al., 2019b; Mlyneczek et al., 2022; Zhang et al., 2023). The intra-
54 annual variations mainly include annual (AO), semi-annual (SAO), and ter-annual (TAO) oscillations. These variations are
55 mainly cause by the revolution of earth with oblique axis relative to the ecliptic plane. Their amplitudes depend on latitude
56 and height (Dunkerton, 1982; Garcia et al., 1997; Randel et al., 2004; Smith et al., 2017).

57 The inter-annual variations are mainly caused by the coupling among different atmospheric layers, sea surface
58 temperature and solar activity. Such as: the QBO (quasi-biennial oscillation) in the tropical regions has periods of 2–3 years
59 due to wave-mean flow interactions. Recently, Pukite et al. (2018) proposed that the QBO signal in the stratosphere can be
60 generated by the modulo aliasing between nodal lunar cycle (27.2122 days) and seasonal impulse signals. Especially, the
61 modulo aliasing between the lunar cycle and an annual impulse can result in a signal with periods of 2.3 years, which is close
62 the QBO periods of 2–3 years (Baldwin et al., 2001). The QBO signal can also be seen in the mesosphere, which is anti-
63 phase to the stratospheric QBO due to the selective critical-layer filtering (Baldwin et al., 2001; Burrage et al., 1996; Xu et

64 al., 2007). Recent studies revealed that the mesospheric QBO is a seasonally locked phenomenon and occurs only in vernal
65 equinox when the westward winds enhanced every 2 or 3 years and might be an ephemeral phenomenon (Venkateswara Rao
66 et al., 2012; Kumar, 2021). The ENSO (El Niño/Southern Oscillation) is used to characterize the changes in sea surface
67 pressure and temperature (Domeisen et al., 2019). It has been reported that the slight change of ENSO can affect global
68 middle and upper atmosphere through the coupling of atmosphere and ocean and wave propagation (Baldwin and O'Sullivan,
69 1995; Randel et al., 2009; Li et al., 2013; Lin and Qian, 2019). The solar activity can be represented by its radiation flux at
70 10.7 cm (F10.7), it can influence the atmosphere from upper to below through photon absorption and high energy particle
71 precipitation and ion deposition (Li et al., 2011; Beig et al., 2008; Qian et al., 2019; Venkat Ratnam et al., 2019). Moreover,
72 the temporal variations may be coupled among different time scales. Such as: the coupling between SAO and QBO is mainly
73 due to the selectively filtering and absorbing of equatorial waves and gravity waves by QBO winds (Li et al., 2012; Smith et
74 al., 2017); the coupling between QBO and ENSO is mainly due to the stronger wave activity in the warm phase ENSO (i.e.,
75 El Niño), this accelerates the downward propagation of QBO (Domeisen et al., 2019; Taguchi, 2010).

76 The variations and responses of temperature and trace gases (e.g., CO₂, H₂O) in the middle and upper atmosphere have
77 been well studied through observations and model simulations (Emmert et al., 2012; Yue et al., 2015, 2019a; Laštovička,
78 2017; Lübken et al., 2008; Garcia et al., 2019; She et al., 2019; Yuan et al., 2019; Mlynčzak et al., 2022). In contrast, the
79 variations and responses of wind field are more complex than those of temperature due to the direct external forcings and the
80 indirect dynamical coupling between waves and mean flow (Qian et al., 2019). In fact, wind field is an important
81 atmospheric parameter since it is a direct driver of atmospheric circulation and influences the atmospheric structure.
82 Moreover, wind field plays important roles in transporting mass and chemical species, in distributing and re-distributing
83 momentum and energy, and in modulating the propagation and dissipation of atmospheric waves (i.e., gravity waves, tides,
84 and planetary waves). This in turn affects the atmospheric circulation and structure indirectly. Thus, the variations and long-
85 term variations of winds should also be studied.

86 Ground-based radar observations have revealed long-term variations of mean wind in the mesosphere and lower
87 thermosphere (MLT) region at several stations. The medium frequency (MF) radar observations at Tirunelveli (8.7°N,
88 77.8°E) from 1993 to 2006 showed that the monthly mean zonal wind was dominated by SAO with eastward peak during
89 solstice and exhibited QBO signal with periods 2–3 years (Sridharan et al., 2007). Using the observations by four MF radars
90 and three meteor radars in the latitudes from 21°S to 22°N during 1990–2010, Venkateswara Rao et al. (2012) showed that
91 the zonal wind exhibited both negative and positive trends, which magnitudes depended on stations and the temporal
92 intervals of the observations. By combining the zonal wind at $\sim z=70\text{--}80$ km observed by rocketsondes, satellite and MST
93 radar over the Indian region (8.5°N to 18.5°N and 69°E to 89°E), Venkat Ratnam et al. (2013) constructed a long-term
94 dataset from 1977 to 2010. They showed a decreasing trend of $2\text{ ms}^{-1}/\text{Year}$ (or $20\text{ ms}^{-1}/\text{Decade}$) in February and March at
95 72.5 and 77.5 km (Fig. 2 of their paper). However, the trends are not significant from May to August. These observations
96 coincided with the results simulated by the Thermosphere-Ionosphere-Mesosphere-Electrodynamics General Circulation
97 Model (TIME-GCM) after doubled the CO₂ concentration (Venkat Ratnam et al., 2013). Recently, after extending the
98 observation data to 2016, Venkat Ratnam et al. (2019) found a decreasing trend at $\sim z=60\text{--}80$ km and an increasing trend of
99 $4\text{--}5\text{ ms}^{-1}/\text{Decade}$ at $\sim z=80\text{--}90$ km and below ~ 60 km. Using the temperature and wind simulated by Whole Atmospheric
100 Community Climate Model with eXtended thermosphere and ionosphere (WACCM-X) and the radar observations at Collm
101 (51°N, 13°E) during 1980–2014, Qian et al. (2019) showed that the zonal wind trends and the solar effects were, respectively,
102 order of $\sim \pm 5\text{ ms}^{-1}/\text{Decade}$ and $\sim \pm 5\text{ ms}^{-1}/100\text{SFU}$ ($1\text{ SFU}=10^{-22}\text{ Wm}^{-2}\text{Hz}^{-1}$) but with large standard deviations. Using the
103 historical simulations by WACCM6 during 1850–2014 (165 years), Ramesh et al. (2020) showed the responses of the
104 temperature and zonal wind to QBO, ENSO, solar activity, ozone depleting substance, carbon dioxide, and aerosol from the

105 stratosphere to the lower thermosphere. They showed that the influences of solar activity are mainly in the mesosphere while
106 the influences of QBO and ENSO are mainly in the stratosphere and mesosphere. Moreover, these influences depend on
107 latitudes.

108 The above observations and modelling studies revealed seasonal variations of zonal winds and their responses to QBO,
109 ENSO, solar activity in the mesosphere. However, the reported long-term (or linear) changes of zonal winds depended on
110 specific locations and the temporal intervals of the data. At present, it is still a challenge to directly measure the atmospheric
111 wind field from the stratosphere to the lower thermosphere. It is compelling to develop a wind dataset to represent the main
112 features of global zonal winds and their temporal variations.

113 Recently, we developed a dataset of global monthly zonal mean zonal wind (short for BU) based on the gradient
114 balance wind theory (Randel, 1987; Fleming et al., 1990; Xu et al., 2009a; Smith et al., 2017) and the temperature and
115 pressure profiles measured by the Sounding of the Atmosphere using Broadband Emission Radiometry (SABER) instrument
116 (Russell III et al., 1999). To overcome the tidal alias above 80 over the equator (Hitchman and Leovy, 1986; Xu et al.,
117 2009b; Smith et al., 2017), we replaced the BU with the zonal wind observed by a meteor radar at Koto Tabang (0.2°S,
118 100.3°E) (Hayashi et al., 2013; Matsumoto et al., 2016). The BU covers a latitude range of 50°S–50°N with step of 2.5° and
119 height range 18–100 km with step of 1 km and a temporal range of 2002–2019. The BU coincides generally with re-analysis
120 data, empirical wind models and observations by meteor radars and lidar (Liu et al., 2021) and with the balance wind derived
121 by Smith et al. (2017) above the equator region. Thus, we focus on variations and responses of global zonal winds to various
122 factors since the BU is a reasonable candidate to monthly mean zonal wind.

123 The solar activity effects on zonal winds in the MLT region are still unclear (Venkateswara Rao et al., 2012; Qian et al.,
124 2019). It should be noted that the linear changes and solar activity have influences on the other signals (i.e., QBO, ENSO),
125 one must isolate the contributions of different signals to get a clearer picture of the variations and responses of zonal winds.
126 The long temporal (18-year) and entire height (18–100 km) intervals of BU are suitable to study the variations of zonal
127 winds and their responses to QBO, ENSO, and solar activity. To separate the relative contributions of the variations and
128 effects of QBO, ENSO, and solar activity on zonal winds, the multiple linear regression (MLR) method will be used.

129 To evaluate the reliability of BU and the corresponding responses below 70 km in further, we will perform the same
130 MLR on the zonal wind of Modern-Era Retrospective analysis for Research and Applications, version 2 (MERRA2). The
131 BU will provide the unique wind results at 70–100 km. MERRA2 provides assimilated meteorological field from surface to
132 ~75 km (72 levels). It has temporal, longitude, and latitude interval of 3 hours, 0.625°, and 0.5°, respectively (Molod et al.,
133 2015; Gelaro et al., 2017). Each MERRA2 zonal wind profile is interpolated to uniform vertical grid with a step of 1 km.
134 Then the monthly zonal mean wind (MerU) is calculated by averaging these profiles in a latitude band of 5° with an overlap
135 of 2.5° in each month. The variations of MerU and their responses to QBO, ENSO, and solar activity are used to compare
136 with those of BU below 70 km. MERRA2 is used here due to its good consistency with other data set. Such as the
137 consistency of the monthly mean zonal winds between MERRA2 and the QBO wind at Singapore (Coy et al., 2016), the
138 consistency of the changes in subtropical and polar jets between MERRA2 and other re-analyses (e.g., MERRA, ERA-
139 Interim, JRA-55, and NCEP CFSR) (Manney and Hegglin, 2018).

140 **2 Data and multiple linear regression**

141 **2.1 BU data and reference time series**

142 The detailed description and validation of BU can be found in (Liu et al., 2021). Here, we provide a short summary of
143 this dataset. The BU dataset includes the monthly mean zonal wind in the height range of 18–100 km with step of 1 km and
144 at latitudes of 50°S–50°N with step of 2.5° from 2002 to 2019. BU is mainly derived from the temperature and pressure

145 observations by the SABER instrument (Russell III et al., 1999) and based on the gradient wind theory (Fleming et al., 1990;
 146 Randel, 1987; Xu et al., 2009a; Smith et al., 2017),

$$147 \frac{\bar{u}^2}{a} \tan \varphi + f\bar{u} = -\frac{1}{a\bar{\rho}} \frac{\partial \bar{p}}{\partial \varphi} \quad (1)$$

148 Here, $f = 2\Omega \sin \varphi$ is the Coriolis factor, $\Omega = 2\pi/(24 \times 60 \times 60)$ is the earth rotation frequency (unit of $\text{rad}\cdot\text{s}^{-1}$), a is the
 149 radius of the earth. \bar{u} and $\bar{\rho} = \bar{p}/R\bar{T}$ are the BU and zonal mean density, respectively. R is the gas constant for dry air. At
 150 the equator and above 80 km, the tidal alias on gradient wind is replaced by the monthly mean zonal wind measured by a
 151 meteor radar at 0.2°S (Hayashi et al., 2013; Matsumoto et al., 2016). Equation (1) is used to calculate the BU in the latitude
 152 ranges of 10°N – 50°N and 10°S – 50°S . Above the equator, the BU is calculated as $\bar{u} = -(\partial^2 \bar{p}/\partial \varphi^2)/(2\Omega a \bar{\rho})$ (Fleming et al.
 153 1990; Swinbank & Ortland, 2003). At 2.5°N – 7.5°N and 2.5°S – 7.5°S , the BU is estimated by a cubic spline interpolation of
 154 the BU at 10°N – 50°N , 10°S – 50°S and the reconstructed BU at the equator. The detailed description can be found in Liu et al.
 155 (2021).

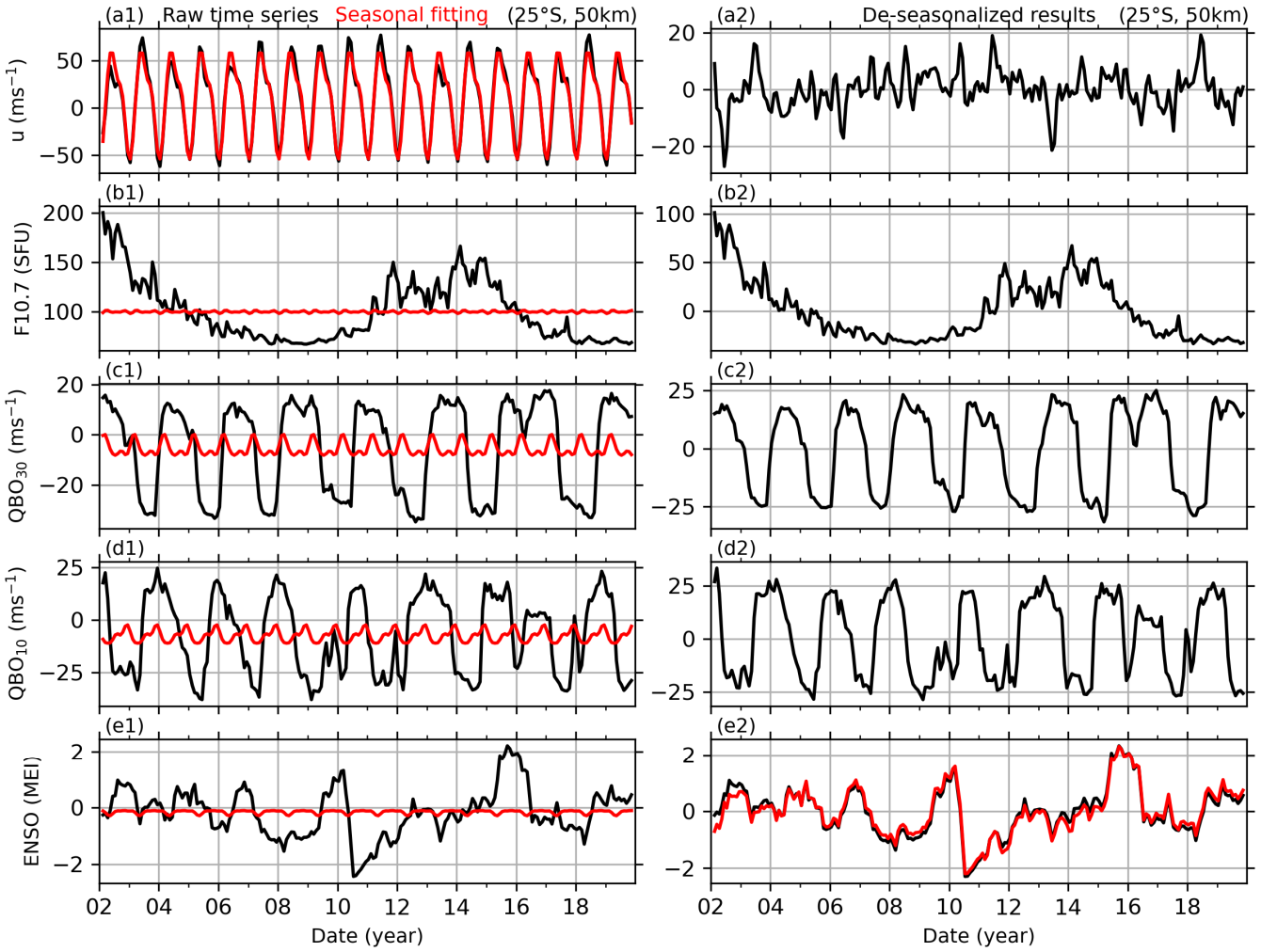


Figure 1: Example of BU and the reference time series (left column) and their de-seasonalized results (right column). The first row: BU at 25°S and 50 km (black line in a1) and its seasonal fitting result (red line in a1), and the de-seasonalized BU (black line in a2). The second, third, and fourth rows: same captions as the first row but for solar activity (indicated by F10.7), QBO at 30 hPa (QBO₃₀ or QBOA) and 10 at hPa (QBO₁₀ or QBOB), and ENSO (indicated by MEI index). The red line in e2 is the residual of MEI index after removing the response of MEI to F10.7.

156 For the consistency of BU and the monthly averaged zonal wind observed at a single station, Figure 3 of Smith et al.
 157 (2017) showed that the monthly zonal wind from a meteor radar at Ascension Island (8°S) coincides well with the BU at 81
 158 and 84 km. This indicates that the monthly averaged zonal wind at a single station can represent the zonal average at least

159 below 84 km. While above 84 km, Fig. 2(a) of Liu et al. (2021) shows that the theoretical balance winds are mainly eastward.
 160 In contrast, the reconstructed winds (Fig. 2b and 2c of Liu et al. (2021)) from a meteor radar observation at Koto Tabang
 161 (0.2°S) are mainly westward. The differences between the theoretical balance wind and meteor radar observations are mainly
 162 due to the tidal aliasing above 84 km (Hitchman and Leovy, 1986; Xu et al., 2009b; Smith et al., 2017). The comparisons
 163 between BU and other data (MERRA2, HWM14 empirical model, meteor radar and lidar observations at seven stations from
 164 around 50°N to 29.7°S) illustrate good agreement. The good agreement suggests that BU is a reasonable candidate to
 165 monthly mean zonal wind. The large vertical extent and the 18-year internally consistent time series of BU makes it is
 166 suitable to study the variations and responses to solar activity, and QBO, ENSO.

167 The reference time series of solar activity, QBO, and ENSO are used to explore their possible influences on global
 168 zonal wind. The solar activity is represented by the solar radio flux at 10.7 cm in a 100-MHz band (F10.7, Fig. 1b1, Tapping,
 169 2013). The QBO is represented by the zonal wind at 30 hPa (~25 km) and 10 hPa (30 km) (referred as QBOA and QBOB in
 170 Fig. 1c1 and 1d1, respectively) over Singapore (1°N, 104°E) (Baldwin et al., 2001). Due to the propagation nature of QBO
 171 with height, we use the QBO winds at two different heights to represent the phase information of QBO. ENSO is represented
 172 by the Multivariate ENSO index (MEI, Fig. 1e1, Zhang et al., 2019; Wolter and Timlin, 2011). These reference time series
 173 play important roles in studying the atmospheric coupling and have been widely used to study their influences on
 174 temperature, gravity waves, ozone, and carbon dioxide in the stratosphere and mesosphere (Randel and Cobb, 1994; Li et al.,
 175 2011; Yue et al., 2015; Liu et al., 2017; Randel et al., 2017).

176 2.2 Multiple linear regression

177 The detailed applications of MLR to retrieve the seasonal variations of winds and the responses of winds to F10.7,
 178 QBOA, QBOB, and MEI can be ascribed to the following three steps. For illustrative purpose, the BU at 25°S and 50 km
 179 (black in Fig. 1a1) is taken as an example to show the procedure of MLR. This procedure is also applied to winds at other
 180 latitudes and heights, but results in different regression coefficients due to the latitudinal and height dependencies of the
 181 seasonal variations and the responses of winds to F10.7, QBOA, QBOB, and MEI.

182 First, we de-seasonalize the wind and reference time series by fitting the following harmonics through the least squares
 183 method. At each latitude and height, the wind series is fitted as,

$$184 \quad u(t_i) = u_0 + \sum_{k=1}^3 A_k \cos[k\omega(t_i - \varphi_k)] + u_{res}(t_i). \quad (2)$$

185 Here, t_i ($i = 1, 2, \dots, N$) is the month number since February 2002. u_0 is the mean wind over the entire temporal interval,
 186 u_{res} is the de-seasonalized wind. $\omega = 2\pi/12$ (month), A_k and φ_k are the amplitude and phase of the annual (AO, $k = 1$),
 187 semi-annual (SAO, $k = 2$), and ter-annual (TAO, $k = 3$) oscillations, respectively. In the same way, Eq. (2) is used to de-
 188 seasonalize the reference time series of F10.7, QBOA, QBOB, and MEI (shown in the left column of Fig. 1), and thus their
 189 de-seasonalized results ($F10.7_{res}$, $QBOA_{res}$, $QBOB_{res}$, MEI_{res} , shown in the right column of Fig. 1) can be obtained and will
 190 be used as predictor variables (or explanation variables).

191 The rationality or goodness of the seasonal fitting result is quantified by R^2 score, which is the variations of the raw
 192 data explained by the model and defined as follows:

$$193 \quad R^2 = 1 - \{\sum_{i=1}^N u_{res}^2(t_i) / \sum_{i=1}^N [u(t_i) - \bar{u}]^2\}, \quad \bar{u} = \frac{1}{N} \sum_{i=1}^N u(t_i). \quad (3)$$

194 The best fitting results in $R^2 = 1$, which means that the fitting result is the same as the raw data. For example, the seasonal
 195 fitting of BU at 25°S and 50 km is shown as red line in Fig. 1(a1). It coincides well with the raw BU series (black line in Fig.
 196 1a1) with $R^2 = 0.967$. This means that Eq. (2) explains 96.7% of the variations of BU at 25°S and 50 km. Moreover, for this
 197 case, the fitting result shows that the AO has amplitude of 53.9 ms^{-1} and is in the dominant position. Then the SAO has a
 198 smaller amplitude of 13.2 ms^{-1} . While the TAO is the weakest and has a amplitude of 3.9 ms^{-1} . The rationality of the fitting
 199 results (R^2) at other latitudes and heights will be shown in Sect. 3.1.

200 Second, we check the multicollinearity among the predictor variables, which are the de-seasonalized F10.7, QBO₃₀,
 201 QBO₁₀, and MEI. The multicollinearity often leads to meaningless results if the correlation coefficients (CCs) between two
 202 or more predictor variables are significant. Here we calculate the CC and p-value of each pair of predictor variables (Table
 203 1). If the p-value of a pair is less than 0.1 (or 0.05), one can state that the CC of this pair differs from zero at a confidence
 204 level 90% (or 95%). And thus, the multicollinearity of this pair is significant. In contrast, larger p-values indicate lower
 205 confidence level and insignificant multicollinearity. Table 1 shows that the CCs of most pairs are less than 0.1, and their p-
 206 values are larger than 0.1. This indicates that the multicollinearities of these predictor variables are insignificant and are
 207 approximately independent. On exception is the pair of F10.7 and ENSO, which has a CC of 0.2022 with p-value of 0.0030.
 208 This indicates that the multicollinearity of F10.7 and ENSO is significant at confidence level of 95%. To improve the
 209 independency between F10.7 and ENSO, a linear regression is performed with response variable of MEI index and predictor
 210 variable of F10.7. The residual of MEI index, which excludes the influences of F10.7, is used as a predictor variable to
 211 represent the effects of ENSO in the following MLR model. We note that the residual of MEI index is still noted as MEI_{res}
 212 in the following text. Now, the multicollinearity among the four predictor variables can be neglected and ensures a
 213 meaningful result of MLR in the next step.

214 **Table 1:** The correlation coefficients and their p-values of regressors

	QBO ₃₀		QBO ₁₀		ENSO (MEI indx)	
	CC	p-value	CC	p-value	CC	p-value
F10.7	-0.0283	0.6803	0.0003	0.9965	0.2022	0.0030
QBO ₃₀			-0.0025	0.9705	0.0368	0.5921
QBO ₁₀					-0.0779	0.2567

215 Third, MLR is applied to get the responses of winds (i.e., u_{res} in Eq. 1) to the four predictor variables (F10.7_{res},
 216 QBOA_{res}, QBOB_{res}, MEI_{res}) prepared in the second step. In the MLR model, the response variable is the de-seasonalized
 217 wind (i.e., u_{res} in Eq. 1) at each latitude and height. The MLR model is written as:

$$218 \quad u_{res}(t_i) = \alpha F10.7_{res}(t_i) + \beta_A QBOA_{res}(t_i) + \beta_B QBOB_{res}(t_i) + \gamma MEI_{res}(t_i) + \eta t_i + \varepsilon(t_i). \quad (4)$$

219 The regression coefficients $\alpha, \beta_A, \beta_B, \gamma$ indicate the responses of wind to F10.7, QBOA, QBOB, and MEI, respectively.
 220 The regression coefficient η is the linear variations or long-term trend. $\varepsilon(t_i)$ is the residual of the fitting and can be used to
 221 estimate the standard deviation and p-value of each coefficient with the help of variance-covariance matrix and the student-t
 222 test (Kutner et al., 2004; Mitchell et al., 2015). The monthly responses are obtained by selecting t_i in Eq. (4) only in that
 223 month of each of year. E.g., the response in January can be obtained by selecting the data only in January of each year. The
 224 annual responses are obtained by using all the data during 2002–2019. Figure 2 shows the monthly responses of BU at 25°S
 225 and 50 km to solar activity (a), QBO (b), ENSO (c) and the linear variations of BU (d), as well as their p-values. The error
 226 bars are the confidence interval at 90% confidence level. The responses of BU at 25°S and 50 km to solar activity (Fig. 2a1)
 227 have an annual mean of $-3.2 \text{ ms}^{-1}/100 \text{ SFU}$ with p-value of 0.05, which are mainly contributed from May–August, in which
 228 the negative peaks reach a value of $-10 \text{ ms}^{-1}/100 \text{ SFU}$ in June and July but with larger p-values (Fig. 2a2). In January–April
 229 and September–October, the responses of BU at 25°S and 50 km to solar activity are much weak. This indicates that the
 230 responses of BU at 25°S and 50 km to solar activity are stronger in the boreal summer and weaker in other months but have
 231 larger p-values. The responses of BU at 25°S and 50 km to QBO₃₀ and QBO₁₀ (Fig. 2b1) have annual means of $-1.2 \text{ ms}^{-1}/10$
 232 ms^{-1} (p-value \approx 0.0) and $-0.3 \text{ ms}^{-1}/10 \text{ ms}^{-1}$ (p-value=0.22). The monthly responses of BU at 25°S and 50 km to QBO₃₀ have
 233 negative peaks of $\sim 3\text{--}5 \text{ ms}^{-1}/10 \text{ ms}^{-1}$ (p-value $<$ 0.1) in April–July, when QBO₃₀ reaches its eastward or westward peaks. Thus,
 234 the responses of BU at 25°S and 50 km to QBO₃₀ are strong in the boreal summer. However, the monthly responses of BU
 235 at 25°S and 50 km to QBO₁₀ are much weaker than that to QBO₃₀. The responses of BU at 25°S and 50 km to ENSO (Fig.
 236 2c1) have an annual mean of $-0.31 \text{ ms}^{-1}/\text{MEI}$ (p-value=0.56). The monthly responses of BU at 25°S and 50 km to ENSO

237 have negative peak in May and positive peaks in July and August but have large p-values in May–November. The annual
 238 mean linear variations (Fig. 1h) is of $0.99 \text{ ms}^{-1}/\text{Decade}$ (p-value=0.27). The monthly linear variations of BU at 25°S and 50
 239 km reach a peak of $3 \text{ ms}^{-1}/\text{Decade}$ (p-value<0.2) in May. We note that the linear variation depends highly on the temporal
 240 span of the data and will be discussed in Sect. 4.1.

241 3 Seasonal variations and regression results

242 3.1 Seasonal variations

243 Figure 3 shows the amplitudes and phases of the seasonal variations of BU (upper row) and MerU (lower row). The R^2
 244 scores (the fourth column) of both BU and MerU are larger than 0.8 at latitudes higher than 20°N/S and below 85km. This
 245 indicates that the variations of BU and MerU can be explained well by Eq. (2) and mainly contributed by the seasonal
 246 variations. However, Above 85 km and in the tropical regions, the R^2 scores of BU are less than 0.6. This indicates that the
 247 variabilities of BU are influenced by some other factors, which were not included in Eq. (2). These factors might include (1)
 248 the phase change (eastward peak shifting from winter to summer) of zonal wind caused by the strong gravity waves
 249 dissipation at high latitudes (Liu et al., 2022), (2) the strong tides and short-term variabilities of zonal wind in the equatorial
 250 lower thermosphere (Xu et al., 2009b; Smith et al., 2017), (3) the imperfect BU in the extra-tropical lower thermosphere (Liu
 251 et al., 2021), and (4) the strong QBO signals, which were not included in Eq. (2).

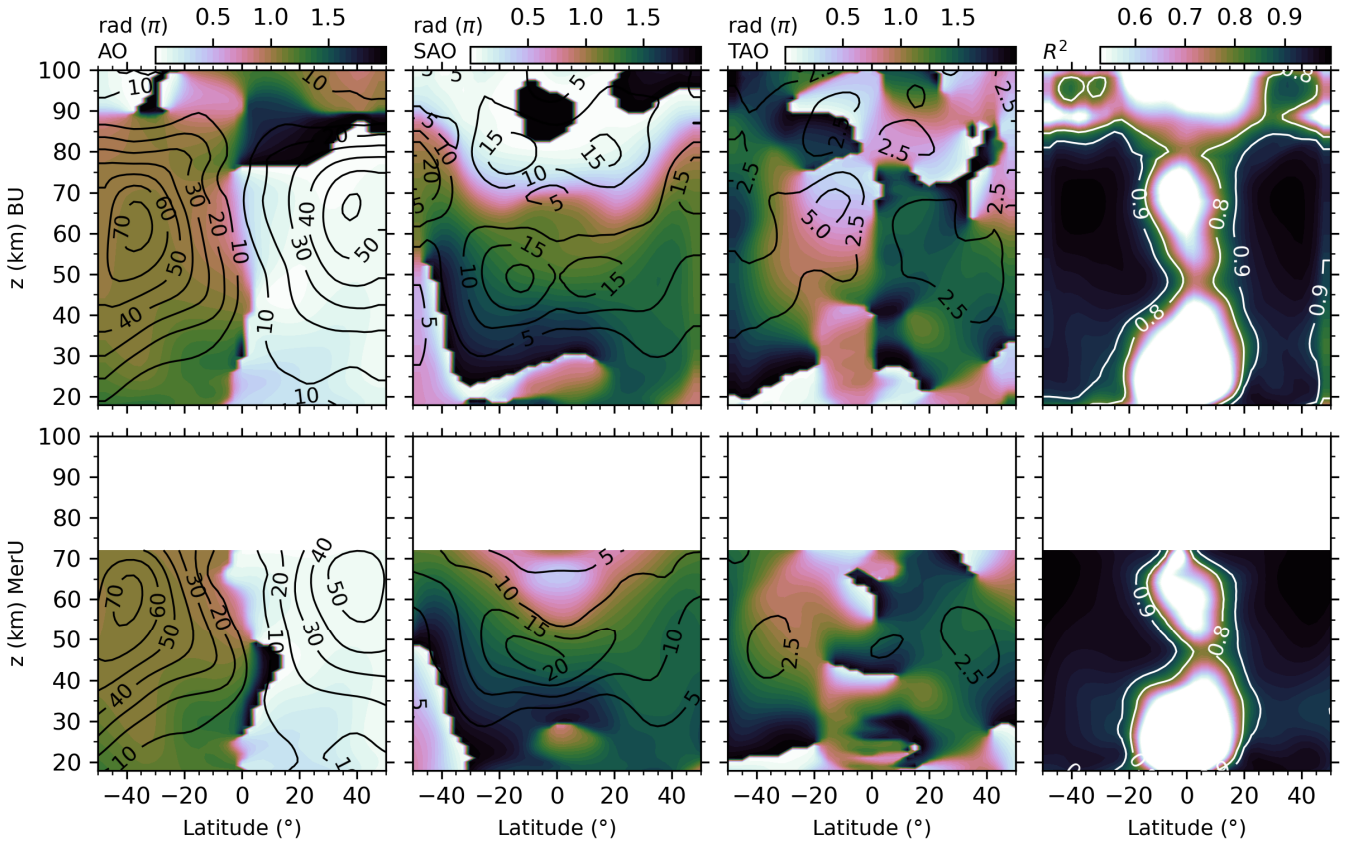


Figure 3: The latitude-height distributions of the amplitudes (contour lines) and phases (color scale) of seasonal variations and the R^2 scores (from left to right) of BU (upper row) and MerU (lower row).

252 The latitude-height distributions of the amplitudes and phases of AOs of BU and MerU exhibit general consistencies
 253 and slight discrepancy. The consistencies include that: (1) both BU and MerU have peaks around 55 km in July in the
 254 Southern Hemisphere (SH) and around 65 km in January in the Northern Hemisphere (NH); (2) both BU and MerU have
 255 small amplitude below ~ 30 km at all latitudes and throughout the height range in the tropical regions. The discrepancy is that

256 the AO of MerU has larger amplitudes in the SH but smaller amplitudes in the NH than that of BU. The possible reason for
257 the weaker AO of MerU in the NH is that it has peak around 65 km, which might be caused by the damping layers of
258 MERRA2 and reduced the zonal wind (Ern et al., 2021). Above 80 km, the amplitude of AO is small. This is because the
259 magnitudes of zonal wind above 80 km are less than those at around 60 km, where the stratospheric polar jet occurs.

260 The SAOs of both BU and MerU have nearly identical phases in the regions where their amplitudes are prominent. The
261 amplitudes of the SAOs of both BU and MerU exhibit hemispheric asymmetry. At latitudes higher than 35°S, the SAOs of
262 both BU and MerU have peaks at $\sim z=35\text{--}55$ km. However, above 65 km, the SAO of BU is stronger than that of MerU. In
263 the tropical regions, the SAOs of both BU and MerU are stronger in the SH than that in the NH. This coincides with the
264 balance wind derived by Nibums-7 Stratospheric and Mesospheric Sounder (Delisi and Dunkerton, 1988), the measurements
265 by High Resolution Doppler Imager (HRDI) measurements, the assimilated data by U.K. Meteorological Office (UKMO)
266 (Ray et al., 1998), and the balance wind derived from SABER and Microwave Limb Sounder (MLS) observations (Smith et
267 al., 2017). Large discrepancies occur at latitudes higher than 40°N, where the SAO of MerU is much stronger than that of
268 BU below ~ 70 km. Above 70 km, the SAO of BU reproduces the same pattern as that at around 40 km but has larger
269 magnitudes and anti-phase.

270 The TAOs of both BU and MerU have same phases and peaks at $\sim z=30\text{--}60$ km and at latitudes higher than 25°S. In the
271 tropical regions and around 45 km, the TAO of BU has two peaks, which are approximately symmetric to the equator, but
272 the TAO of MerU has one peak over the equator. At $\sim z=50\text{--}70$ km, the TAO of BU has larger amplitude than that of MerU.
273 Above 80 km, the TAO of BU is asymmetric to the equator and has larger peak in the SH tropical region.

274 A short summary is that AO, SAO, and TAO of both BU and MerU have nearly identical phases in the regions where
275 their amplitudes are prominent. Their consistencies are better in the SH than in the NH on the aspects of both patterns and
276 magnitudes. The discrepancies of these seasonal variations are mainly in the NH. Above 70 km, the weak AO due to the
277 weaker wind as compared to that in the stratospheric jet region. The SAO of BU around 50 km and 80 km are hemispheric
278 asymmetric and stronger in the SH, which coincides with the HRDI observations (Ray et al., 1998) and the balance winds
279 derived from temperature observations by satellites (Delisi and Dunkerton, 1988; Smith et al., 2017). The TAO of BU above
280 80 km is hemispheric asymmetric and stronger in the SH.

281 3.2 Responses to solar activity

282 The latitude-height distributions of the responses of BU and MerU to F10.7 (upper two rows of Fig. 4) exhibit general
283 consistencies in July and October and in the annual mean. These consistencies include: (1) the negative responses at $\sim 30^\circ\text{S}$
284 and from 20 km to 60 km in July; (2) the negative response around the equator and ~ 40 km in October; (3) the negative
285 response in the SH stratospheric jet region in the annual mean. In contrast, the discrepancies are: (1) stronger negative
286 response (but insignificant) of BU in January at 50°N, as compared to that of MerU; (2) the positive responses of BU in July
287 around 70 km and 20°N/S, and in October around 65 km and above the equator, which cannot be seen in MerU. The annual
288 mean responses of BU and MerU are: (1) mainly negative in the regions extending from $\sim 30^\circ\text{S/N}$ to higher latitudes below
289 ~ 60 km; (2) mainly negative in the tropical regions and around ~ 40 km. Above ~ 80 km, the response of BU to F10.7 is
290 insignificant. The annual mean responses of BU to F10.7 are mainly positive at 60–80 km. This feature has a similar pattern
291 but larger amplitude as compared to the results simulated by WACCM-X (Ramesh et al., 2020).

292 The monthly-height distributions of the responses of BU and MerU to F10.7 (lower two rows of Fig. 4) exhibit general
293 consistencies below ~ 70 km. However, the discrepancies should be clarified. Such as: the stronger negative responses of BU
294 in winter months (June–August at 50°S and December–January at 50°N); the weaker negative responses of BU at ~ 40 km
295 over the equatorial as compared to that of MerU. It should be noted that the negative responses of winds at the southern and

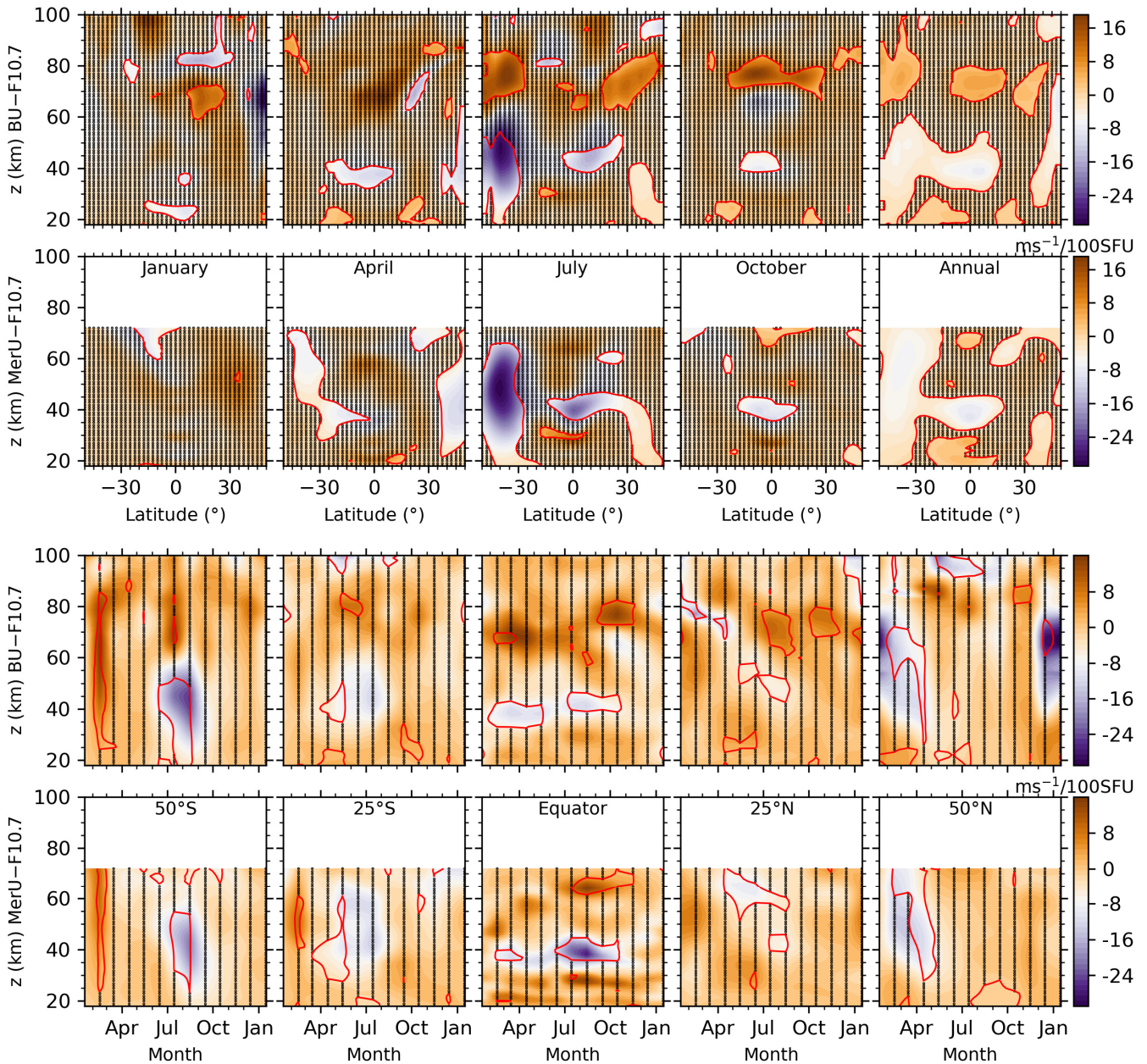


Figure 4: Upper two rows: latitude-height distributions of the regression coefficients of BU (the first row) and MerU (the second row) to F10.7 in January, April, July, October, and annual mean (from left to right). Lower two rows: monthly-height (lower two rows) distributions of the regression coefficients of BU (the third row) and MerU (the fourth row) to F10.7 at 50°S–50°N with interval of 25° (from left to right). The black dots indicate that the regression coefficients with p-values larger than 0.2. The red lines indicate the regression coefficients with p-values of 0.1.

297 The MF radar observations at Langfang (39.4°N, 116.7°E) revealed a positive correlation between zonal wind and solar
 298 activity from 2009 to 2020 during spring and summer at 80–84 km (Cai et al., 2021). However, another MF radar
 299 observations at Juliusruh (54.6°N, 13.4°E) revealed that the correlation between zonal wind and solar activity from 1990 and
 300 2005 were positive during winter but negative in summer (Keuer et al., 2007). Our results coincide with the observations at
 301 Langfang but different from those at Juliusruh. The simulation study by Qian et al. (2019) showed that the solar activity
 302 effects on global zonal wind are sporadic in latitude and height distributions. They suggested that the zonal wind might be
 303 influenced by both the direct effects of solar radiance and the indirect effects of dynamic process such as wave-mean flow
 304 interaction. Another possible mechanism is that the modulation of solar heating is in the ozone layer, which influences the

305 meridional gradient of temperature and thus the zonal wind. However, this mechanism should be validated through
 306 observations or simulations. Qian et al. (2019) also proposed that the temporal intervals of data should be specified when we
 307 study the trends and solar activity effects since the trend drivers are different in different periods. This will be discussed in
 308 Sect. 4.1.

309 A short summary is that the annual mean responses of both BU and MerU to F10.7 are more negative in the
 310 stratospheric polar jet region of SH than that of NH. Above the stratospheric polar jet, the responses of BU change from
 311 negative to positive with the increasing height. Around ~ 80 km, the annual responses of BU to F10.7 are mainly positive in
 312 the tropical region and in the high latitudes.

313 3.3 Responses to QBO

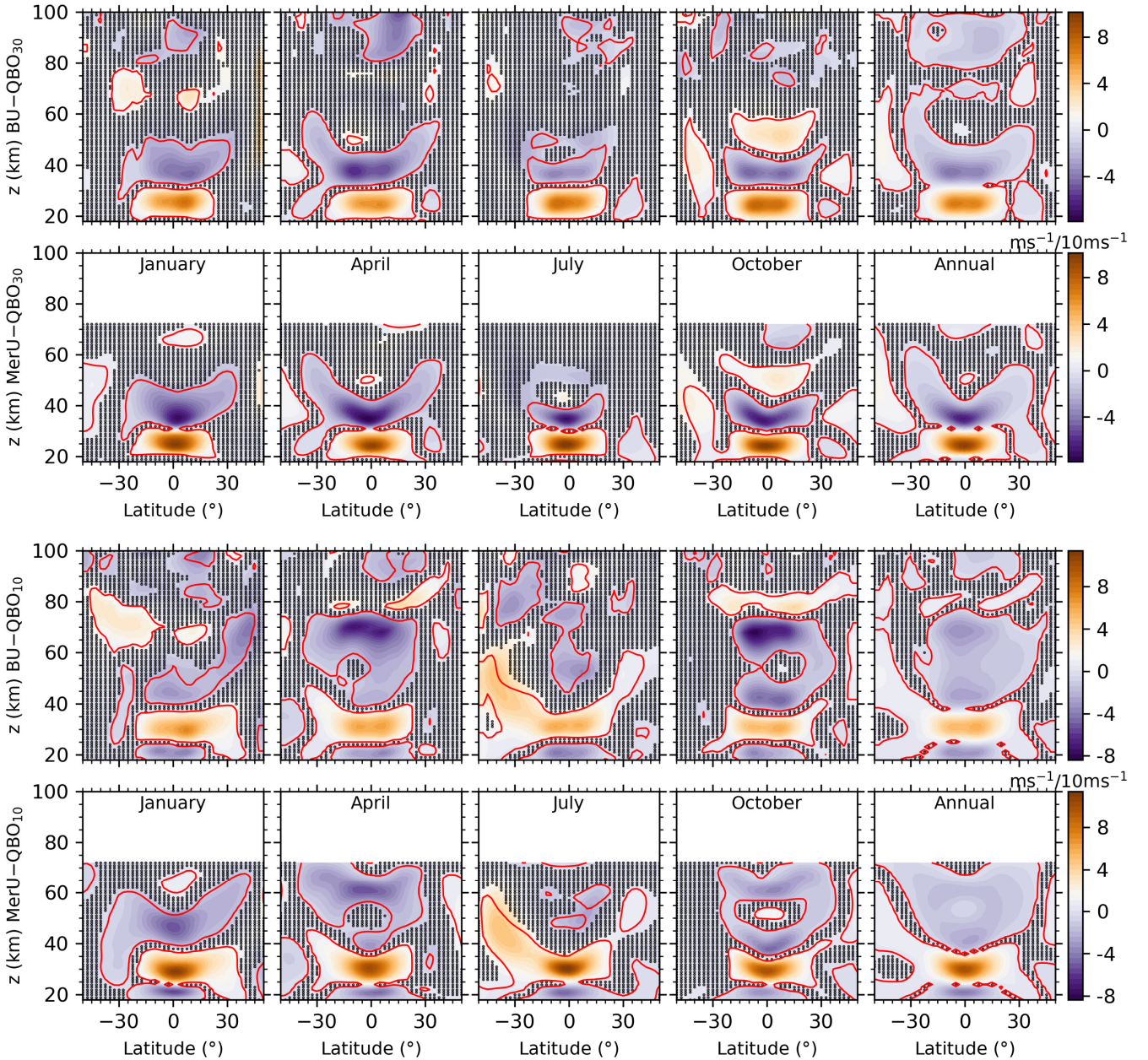


Figure 5: Same captions as the upper two rows of Fig. 4 but for the responses to QBO_{30} (QBOB, upper two rows) and QBO_{10} (QBOB, lower two rows).

314 The latitude-height distributions of the responses of BU and MerU to QBO_{30} (upper two rows of Fig. 5) exhibit general

315 consistencies in all months and in the annual mean below ~ 50 km. Such as the responses of BU and MerU to QBO₃₀ change
316 from positive below 30 km to negative at $\sim z=30\text{--}50$ km and $25^\circ\text{S}\text{--}25^\circ\text{N}$. The varying responses with height are mainly due
317 to the downward propagation of QBO phase with time. This can be confirmed by the responses of BU and MerU to QBO₁₀ at
318 a higher height (lower two rows of Fig. 5), where the responses of BU and MerU to QBO₁₀ change from negative to positive
319 and then negative again. The discrepancy is that the responses of BU to QBO₃₀ and QBO₁₀ are slightly weaker than those of
320 MerU below ~ 50 km.

321 The responses of BU to QBO₃₀ are weaker at $\sim 50\text{--}80$ km. As the height increases, the responses of BU to QBO₃₀
322 become stronger again and have peak around ~ 90 km. This coincides with the mesospheric QBO, which is anti-phase with
323 the stratospheric QBO and extends to $30^\circ\text{S}\text{--}30^\circ\text{N}$ as revealed by High Resolution Doppler Imager observations (HRDI)
324 (Burrage et al., 1996), TIMED Doppler Interferometer observations (Kumar, 2021) and reviewed by Baldwin et al., (2001).
325 This coincides also with the results simulated by WACCM6 on the aspects of the hemispheric asymmetry, i.e., the responses
326 extending to higher latitudes in winter hemisphere (Ramesh et al., 2020). Moreover, the annual mean responses of BU and
327 MerU to QBO₃₀ and QBO₁₀ are positive and are significant at 50°S at $\sim z=50\text{--}80$ km. In contrast, the responses of winds to
328 QBO₃₀ and QBO₁₀ are negative and have smaller regions with p-values less than 0.1. The significant positive responses at
329 50°S are mainly contributed by those in July and October around 50 km, where and when the stratospheric polar jet occurred.

330 A short summary is that the influences of the stratospheric QBO extend from the equator to higher latitudes. The
331 influences can be positive or negative, which depend on heights and latitudes. Such as the negative influences above ~ 80 km
332 in the tropical region and the positive influences at the southern high latitudes. Above ~ 80 km, the negative responses of
333 winds to the stratospheric QBO are hemispheric asymmetry and are more negative in the NH tropical regions.

334 3.4 Responses to ENSO

335 The latitude-height distributions of the responses of BU and MerU to MEI (upper two rows of Fig. 6) generally coincide
336 with each other in all months and in the annual mean. In January and at $\sim z=40\text{--}60$ km and latitudes higher than 40°N , the
337 responses of MerU and BU to MEI are not significant. This coincides with the results simulated by WACCM6, which were
338 positive but were lower than the 95% confidence level (Ramesh et al., 2020). In April and October, and at ~ 35 km, the
339 negative responses of winds to MEI are approximately hemispheric symmetric. The annual mean responses of both winds to
340 MEI are stronger and wider in the SH than those in the NH. In July and at ~ 50 km, the responses of both winds are positive
341 with peaks around $\sim 40^\circ\text{S}$. This indicates that the positive MEI index (warm phase of ENSO or El Niño event) increases the
342 eastward zonal winds. Above 60 km, the positive responses of winds to MEI tilt from higher height (~ 90 km) at 35°S to a
343 lower height (~ 80 km) at 35°N in January. This pattern continues in April and July but is insignificant. Above ~ 90 km and
344 around $\sim 15^\circ\text{S}$, the responses of BU to MEI are positive in January and negative in July. The annual mean responses are
345 mainly positive in most latitudes.

346 The monthly-height distributions of the responses of BU and MerU to MEI (lower two rows of Fig. 6) generally
347 coincide with each other at each latitude, except that the responses of BU to MEI have stronger peaks than those of MerU at
348 50°N/S . The prominent responses of winds to MEI are positive at 50°S (tilting from July at higher height to October at lower
349 height) and are negative at 50°N (mainly in March and April). At 25°N/S , the responses of winds to MEI are mainly positive
350 (extending upward to ~ 50 km and then tilting backward with the increasing height in July and August) and are negative
351 (extending backward and forward below ~ 60 km). At the equator, the responses of MerU to MEI exhibit larger variabilities
352 than those of BU below ~ 40 km.

353 Previous studies showed that during El Niño (warm phase of ENSO), the warm sea surface temperature increases the
354 wave activity, which has a high probability of leading to sudden stratospheric warming (SSW) events (Polvani and Waugh,

355 2004). Then the warm temperature and decelerated zonal wind anomalies can be observed in the stratosphere from January
 356 to April at 60°N (Manzini et al., 2006; Domeisen et al., 2019). This can be summarized as a negative response of zonal wind
 357 to ENSO at northern high latitudes. This negative response can also be seen at 50°N (lower-right two panels of Fig. 5). Using
 358 the WACCM simulations and SABER observations, Li et al., (2016) showed that the stratospheric zonal wind is weekend
 359 due to the increased stratosphere meridional temperature gradient at the southern high latitudes in December and in the warm
 360 phase of ENSO. This supports the weak negative responses of zonal wind to ENSO at 50°S in December (lower-left two
 361 panels of Fig. 6). However, Both BU and MerU showed that the responses zonal wind to ENSO are positive from July to
 362 October at 50°S. The physics behind this positive response should be further explored through simulation studies.

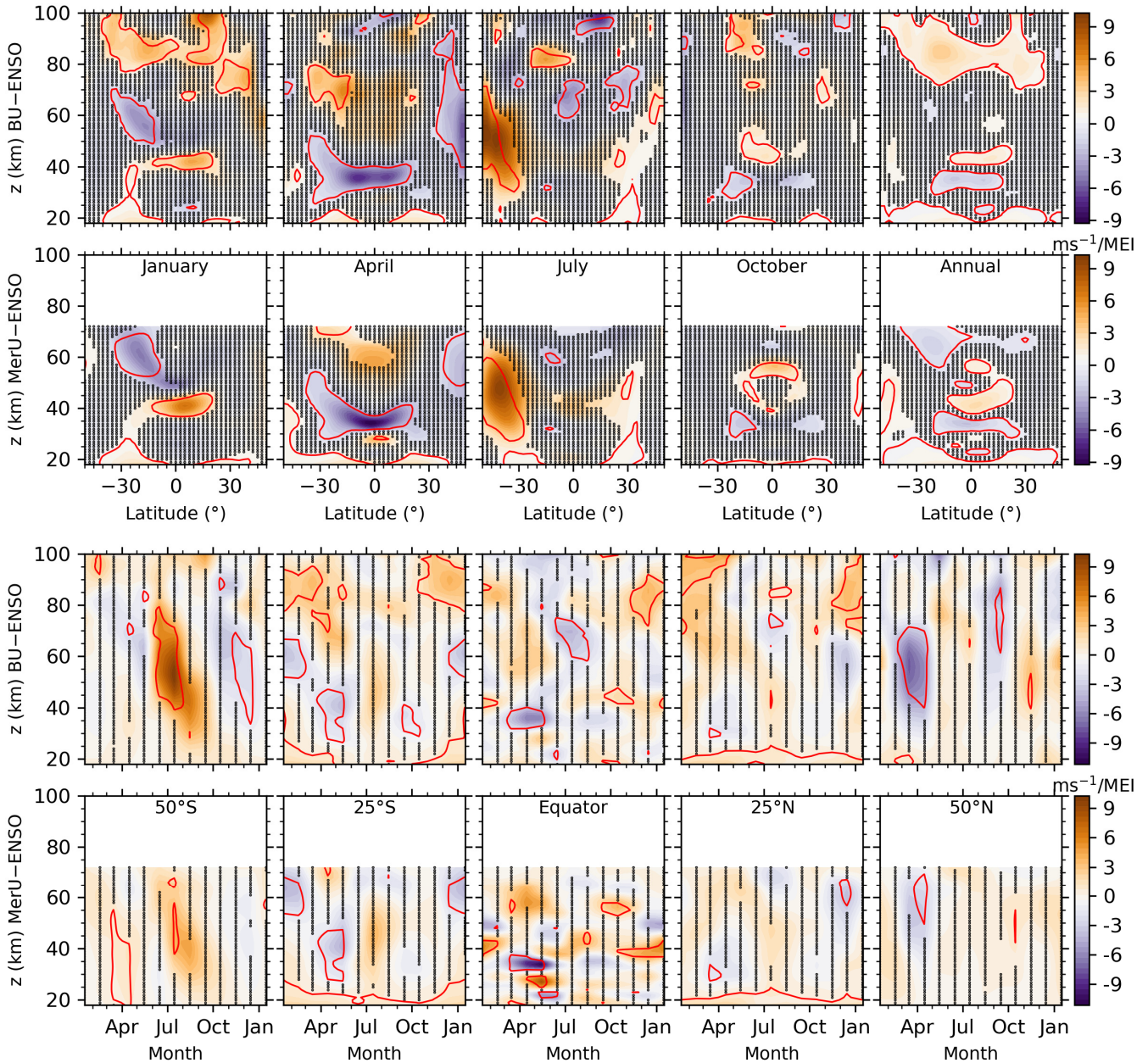


Figure 6: Same caption as Fig. 4 but for the responses to ENSO.

363 It seems unusual that during July in the SH there is a strong signal in both F10.7 and ENSO. A possible reason is that
 364 the waves (gravity waves, non-migrating tides, planetary waves) exhibit stronger variabilities and more complex spatial-
 365 temporal structures in the NH than those in the SH. This induces a more complex dynamical coupling between waves and
 366 zonal mean wind in the NH than that in the SH. Then the complex dynamical coupling might induce that influences of F10.7
 367 and ENSO to wind are not as obvious in the NH as in the SH. Another possible reason is that the zonal mean wind is

368 stronger in the SH than that in the NH during winter times. Thus, the responses of winds to F10.7 and ENSO are stronger
 369 during July in the SH than those in the NH counterpart. Moreover, the responses of winds to QBO₁₀ are also stronger in the
 370 during July in the SH than those in the NH counterpart.

371 A short summary is that both BU and MerU exhibit similar responses to MEI. Whereas the responses of BU to MEI are
 372 stronger than those of MerU at 50°N/S. An interesting feature is that the responses of winds to MEI propagate downward
 373 with increasing time at 50°N/S and 25°N/S, especially the positive responses of BU to MEI at 50°S and 25°S.

374 3.5 Linear variations

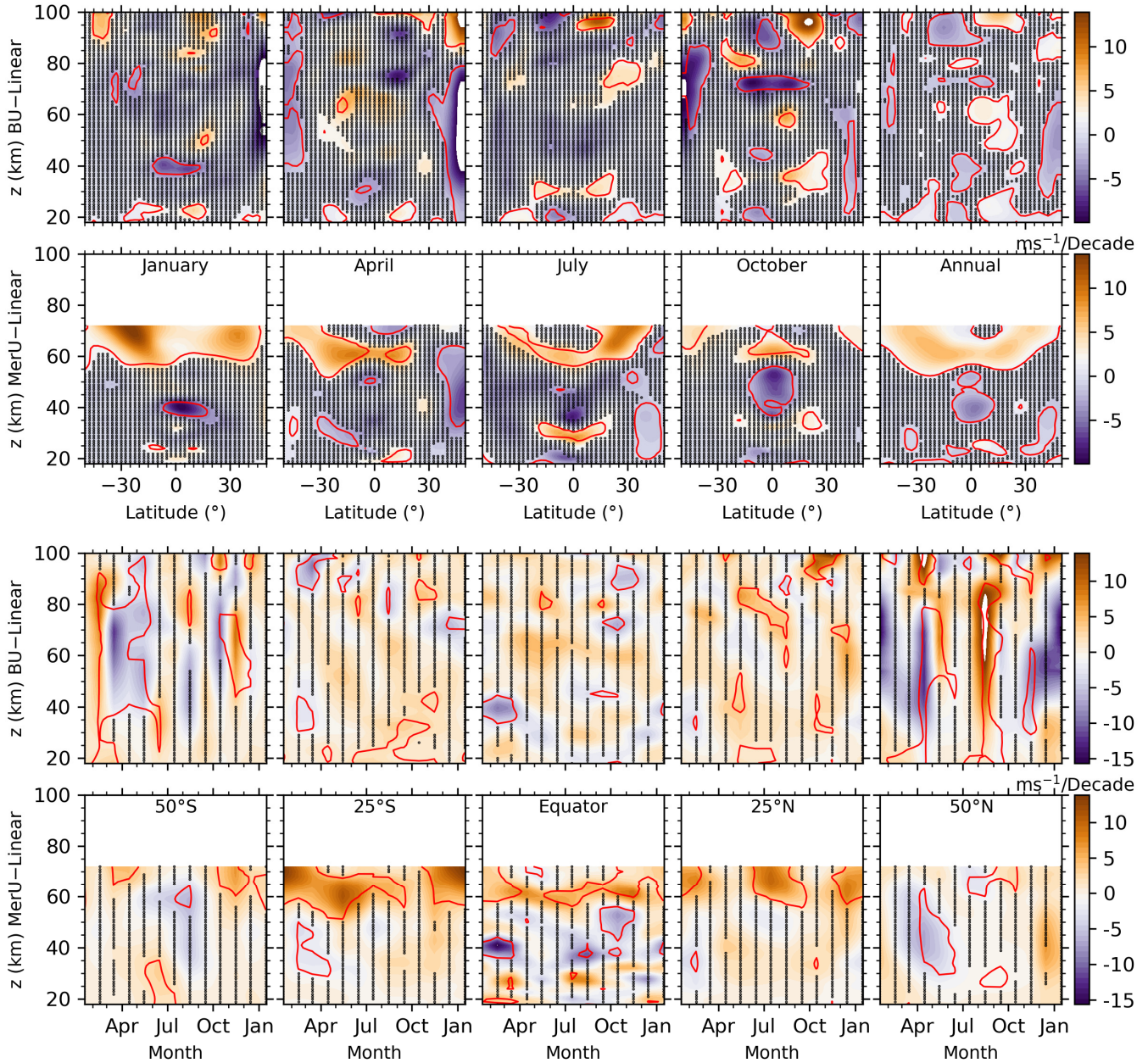


Figure 7: Same caption as Fig. 4 but for the linear variations.

375 The latitude-height distributions of the linear variations of BU and MerU (upper two rows of Fig. 7) generally coincide
 376 with each other in regions with p-values smaller than 0.1. The consistencies include: (1) in January and around the equator,
 377 the negative variations at ~40 km; (2) in April and in the annual mean, the negative variations having peaks at 40°N and
 378 extending to the northern higher latitudes. The discrepancies of the linear variations between BU and MerU include that: (1)
 379 the negative variations of BU around 50°N (50°S) cannot be seen in MerU in January (April); (2) the positive variations of

380 MerU are larger than those of BU above ~ 55 km. Above 70 km, the patterns of the linear variations of BU are sporadic and
381 insignificant and are strongly dependent on months, latitudes and heights.

382 The monthly-height distributions of the linear variations of BU and MerU (lower two rows of Fig. 7) generally coincide
383 with each other. The negative variations of BU and MerU coincide with each other but are insignificant at 50°S in June–
384 August and at 25°S in March–May. However, the large discrepancy is that the negative variation of BU at 50°N (but
385 insignificant) cannot be seen in MerU in October–January. Above ~ 70 km, the positive variations (but insignificant) last a
386 longer time interval as compared to the negative variations.

387 Using the MF radar observations at Juliusruh (54.6°N ; 13.4°E) during 1990–2005, Keuer et al. (2007) showed that the
388 zonal wind below 80 km exhibited a negative trend of $\sim 5 \text{ ms}^{-1}/\text{Decade}$ in summer and a positive trend of $\sim 4 \text{ ms}^{-1}/\text{Decade}$ in
389 winter (Fig. 14 of their paper). This result does not coincide with our analysis. By combining the radar, rocketsondes and
390 satellite observations over Indian region and the simulation results by WACCM-X, Venkat Ratnam et al. (2019) show a
391 negative trend of $\sim 5 \text{ ms}^{-1}/\text{Decade}$ between 70 and 80 km. This result coincides with our analysis only during October. It
392 should be noted that the linear variations of zonal wind depend on the stations, height ranges, measuring techniques, and the
393 temporal intervals of the data (Keuer et al., 2007; Ramesh et al., 2020). This illustrates the complexity of the linear variations
394 of zonal wind. Moreover, the inhibited linear variations of predictors used in the MLR model and the dynamics (such as
395 SSW) are also important in retrieving the linear variations of zonal winds (Qian et al., 2019). The effects of the temporal
396 coverage of the data and SSWs in the NH on the responses will be discussed in Sect. 4.

397 A short summary is that both BU and MerU exhibit similar linear variations. But this consistency is not as good as that
398 the seasonal variations, or the responses to F10.7, QBO, and ENSO. The large discrepancy is that the negative variations of
399 BU at 50°N cannot be seen in MerU in October and January. Above 70 km, the patterns of the linear variations of BU are
400 sporadic and insignificant and are strongly dependent on months, latitudes, and heights.

401 4 Discussions

402 4.1 Influences of temporal intervals of data

403 Robust responses or linear variations should not depend on the temporal intervals of the data (Souleymane et al., 2021;
404 Mudelsee, 2019; Qian et al., 2019). This means that the temporal interval of the data should be long enough, which is
405 difficult to be satisfied since the atmospheric variations or oscillations have multiple temporal scales (ranging from month to
406 decade). To test the robustness of the regression results described in Sect. 3, we change the temporal intervals of both BU
407 and MerU according to solar activity, which exhibits nearly 11-year variations. One is 2002–2015, which covers an interval
408 from solar maximum to minimum and then to maximum. The other is 2008–2019, which covers an interval from solar
409 minimum to maximum and then to minimum. After August 2004, the MLS data have been assimilated into MERRA2
410 (Molod et al., 2015; Gelaro et al., 2017). To test the sensitivity to this change, we introduce the third temporal interval of
411 2005–2019. Finally, the fourth temporal interval is 2002–2019, which is the entire data used here.

412 Figure 8 shows the annual mean responses of winds to QBO_{30} and ENSO in the four temporal intervals. The responses
413 of BU to QBO_{30} (the first row) are nearly identical among the four temporal intervals throughout the height range. The slight
414 difference is the weaker positive responses of BU to QBO_{30} during 2002–2015 and 2002–2019 at ~ 70 km around the equator.
415 The responses of MerU to QBO_{30} (the second row) are also nearly identical among the four temporal intervals throughout the
416 height range. The slight difference is the weaker positive responses (insignificant) of MerU to QBO_{30} at ~ 50 km around the
417 equator during 2005–2019. These comparisons show that the responses of winds to QBO_{30} are robust and are almost
418 independent on the temporal intervals.

419 The annual mean responses of BU to ENSO (the third row) have similar patterns among the four temporal intervals.

Such as: (1) the positive responses extending from the southern lower latitudes at lower height to higher latitudes at higher height, (2) the positive responses extend from the tropical regions at ~ 40 km to middle latitudes at higher height, (3) the positive and negative responses shifting with height in the tropical regions below ~ 40 km. The slight difference is the weaker positive at the southern high latitudes and around ~ 50 km during 2002-2015 and 2002-2019, as compared to the other two temporal intervals. The responses of MerU to ENSO (the fourth row) have also similar patterns of responses among the four temporal intervals. This is similar to that of BU and might be caused by the larger variabilities of MEI index after 2008. The negative responses of both winds to ENSO are stronger around $\sim 20^\circ\text{S}$ and ~ 60 km during 2002-2015 and 2002-2019, as compared to other temporal intervals. In a word, the responses of winds to ENSO are robust but slightly depend on the temporal intervals. We note that the pancake structures in the responses of winds to QBO are likely induced by the propagation nature of QBO. Similar pancake structures can also be seen in the responses of wind to ENSO. Moreover, the pancake structures can also be seen in the responses of the zonal mean temperature to ENSO (Fig. 2 of Li et al. (2013)). The physics behind should be further explored.

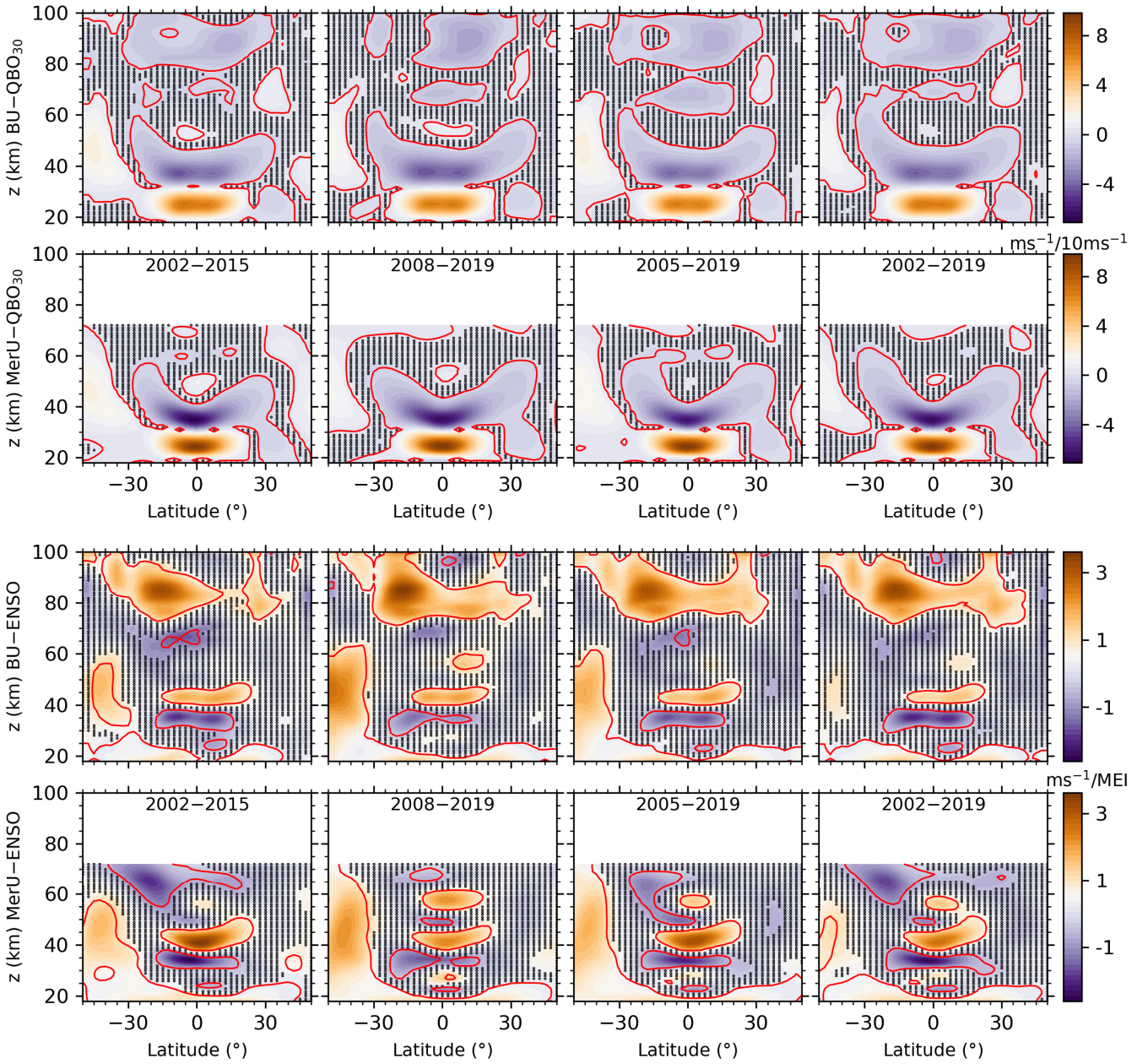


Figure 8: Latitude-height distributions of the annual mean responses of BU (the first and third rows) and MerU (the second and fourth rows) to QBO30 (upper two row) and ENSO (the lower two rows). The black dots indicate where the regression

coefficients with p-values larger than 0.2. The red lines indicate the regression coefficients with p-values of 0.1

432 Figure 9 shows the annual mean responses of winds to F10.7 (upper two rows) and the linear variations of winds (lower
 433 two rows) in the four temporal intervals. In the temporal intervals of 2002–2015 and 2002–2019, both BU and MerU exhibit
 434 similar responses to F10.7. In the temporal intervals of 2008–2019 and 2005–2019, both BU and MerU also exhibit similar
 435 responses to F10.7. In the four temporal spans, the responses of MerU to F10.7 are more negative at latitudes higher than
 436 $\sim 30^\circ\text{S}$ and extend to a higher height than those of BU. Around the tropical region and at ~ 40 km, the responses MerU to
 437 F10.7 are more negative than those BU. At latitudes higher than $\sim 30^\circ\text{S}$ and around the tropical regions, the positive
 438 responses of BU to F10.7 have peaks at $\sim z=70\text{--}85$ km, which are larger in the temporal intervals of 2002–2015 and 2002–
 439 2019, as compared to other temporal intervals. The stronger responses in the temporal intervals of 2002–2015 and 2002–
 440 2019 might be caused by the fact that the solar activity has a higher peak in 2002 than in 2014 (Fig. 1b).

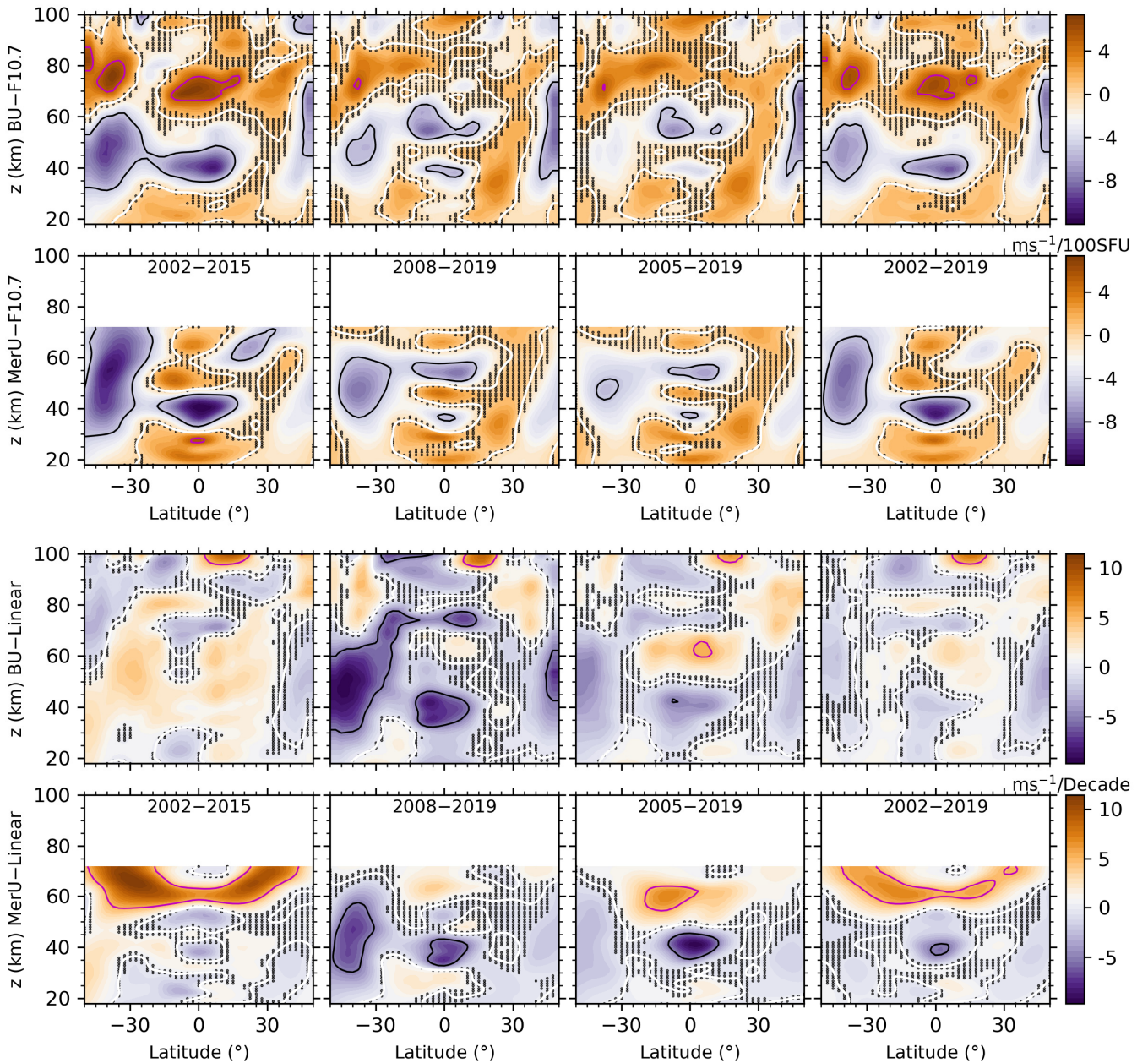


Figure 9: Same caption as Fig. 8 but for the responses to F10.7 (upper two rows) and linear trend (lower two rows).

441 The linear variations of both BU and MerU depend strongly on the temporal intervals and on the values at both edge
 442 points. Among the four temporal intervals, the regions and magnitudes of negative variations are largest and strongest in the

443 temporal span of 2008–2019, and are larger and stronger in the temporal interval of 2005–2019, and then are insignificant in
 444 the temporal interval of 2002–2019. In contrast, the regions and magnitudes of positive variations are largest and strongest in
 445 the temporal interval of 2002–2015. Because the dependencies of the linear variations of BU and their dependencies on
 446 different temporal interval are similar to those of MerU, we cannot determine whether or not the assimilation of MLS data
 447 into MERRA2 influences the linear variations. The possible reasons, which are responsible for the strong dependencies of
 448 the linear variations on different temporal intervals, can be ascribed to the different linear variations inhibited in the
 449 predictors and the unstable predictors in different temporal intervals (Qian et al., 2019).

450 First, we examine the linear variations inhibited in the predictors (F10.7, QBO, and ENSO) and list their linear slopes in
 451 Table 2. The values in Table 2 are approximate values and are derived through the following steps. From the upper two rows
 452 of Fig. 9, we see that the maximum responses of winds to F10.7 is $10 \text{ ms}^{-1}/100\text{SFU}$ ($0.1 \text{ ms}^{-1}/\text{SFU}$). According to this
 453 conversion rule, one unit of the linear variation of F10.7 (SFU/Decade) can induce the wind variation of $0.1 \text{ ms}^{-1}/\text{Decade}$.
 454 Approximately, one unit of the linear variation of ENSO (MEI/Decade) can induce the wind variation of $1 \text{ ms}^{-1}/\text{Decade}$.
 455 Thus, in quality, the combination influences of these regressors can be summarized and listed in the last row of Table 1. We
 456 see that the inhibited linear variations of these regressors provide negative (positive) variations in the temporal spans of
 457 2002–2015 and 2002–2019 (2008–2019 and 2005–2019). These inhibited linear variations share the linear variations of
 458 winds in Eq. (4). The positive (negative) inhibited linear variations make the linear variations winds more negative (positive).
 459 This is confirmed by the fact that the regions and magnitudes of linear variations decrease if we remove the linear variations
 460 of each regressors (not shown here). This explains partially the strong dependencies of the linear variations on different
 461 temporal spans.

462 **Table 2:** Linear variations of F10.7, QBO30, QBO10, and ENSO in different temporal spans and their combination
 463 effects on the linear variations of BU

Regressors (unit)	2002–2015	2008–2019	2005–2019	2002–2019
F10.7 (SFU/Decade)	1.1	-3.2	6.7	-17.3
QBO ₃₀ ($\text{ms}^{-1}/\text{Decade}$)	-2.5	0.7	5.6	1.5
QBO ₁₀ ($\text{ms}^{-1}/\text{Decade}$)	2.2	3.6	3.1	0.1
ENSO (MEI/Decade)	-0.1	1.1	0.5	0.1
Combination ($\text{ms}^{-1}/\text{Decade}$)	-0.29	5.08	9.87	-0.03

464 Second, even if we remove the linear variation of each predictor, the dependencies of the linear variations on different
 465 temporal spans cannot be removed completely. This might be induced by the fact that the predictors are not stable time series
 466 and have varying magnitudes and periodicities in different temporal intervals. Such as the MEI index, which has larger
 467 variabilities after 2009 than before (Fig. 1e); F10.7, which has larger peaks in 2002 than in 2014 (Fig. 1b). It should be noted
 468 that each predictor has its own linear variations and varying magnitudes and periodicities, which are the physical nature of
 469 the predictor and should not be removed. Such that one can get a reliable response of the winds to each predictor although
 470 the responses depend on the temporal interval of the data.

471 The dependencies of winds to QBO are almost identical in different temporal intervals. The dependencies of winds to
 472 ENSO on temporal intervals are slightly stronger than to QBO. The dependencies of winds to F10.7 on temporal intervals
 473 are stronger than to QBO. The dependency of the linear variations of winds on temporal intervals are the strongest one.
 474 Comparing among these responses and the linear variations, we can conclude that the MLR can capture robust responses if
 475 the predictor has relatively stable oscillation period and amplitude (i.e., QBO) and the data length is long enough to cover the

476 main features of the predictor. The robustness decreases as the stability (i.e., the magnitudes and periodicities) of the
477 predictor decreases (such as ENSO and F10.7). For the linear variation, its oscillation period can be regard as infinite. Thus,
478 the data length should be infinite to get a reliable linear variation. However, this is not possible in reality. Consequently, we
479 propose that the linear variations should be examined in different temporal spans, such that one can get a more
480 comprehensive impression on the linear variations although the exact long-term linear variations are unknown.

481 To illustrate the influences on the temporal interval on the linear variations and responses, we performed the MLR
482 procedure on the 40 years (1980–2019) of MERRA2 data (MerU40, not shown here) to the results from 18 years (2002–
483 2019) of MERRA2 data (MerU18). Below ~55 km, which is most reliable height since the damping is significant above this
484 height (Ern et al., 2021), we find that the consistencies of the responses of MerU18 and MerU40 to QBO₃₀ and ENSO are
485 better than those to F10.7 and the linear variations. Moreover, at ~40 km and around the equator, the significant negative
486 linear variations of MerU40 coincide well with those MerU18.

487 **4.2 Possible reasons of hemispheric asymmetry**

488 The responses of both BU and MerU to F10.7 and ENSO exhibit hemispheric asymmetry. Specifically, the negative
489 (positive) responses of winds to F10.7 are stronger in the SH than those in the NH above the stratospheric polar jet region
490 (around 80 km). The responses of winds to ENSO are positive and significant in the SH stratospheric jet region but are
491 negative and insignificant in the NH counterpart. Above 80 km, the responses of BU to ENSO are more positive in the SH
492 sub-tropical region than those in NH counterpart. The positive responses of winds to QBO extend to a wider latitude range in
493 the SH stratospheric jet region than those in the NH counterpart. Moreover, the seasonal and linear variations of BU and
494 MerU also exhibit hemispheric asymmetry. Specifically, the peaks of AO of both BU and MerU have larger amplitudes and
495 at lower heights in SH than those in the NH. Although the linear variations of winds depend on the temporal intervals of data,
496 the linear variations are hemispheric asymmetry on aspects of magnitudes and patterns in each temporal interval.

497 Since the predictor variables are same at all latitudes and heights, the hemispheric asymmetric responses should come
498 from the hemispheric asymmetry of zonal winds. Figures 3 and 4 of Liu et al. (2021) have shown that both BU and MerU
499 were faster in the SH than those in the NH, especially when the wind is eastward in winter of each hemisphere. Moreover,
500 the winds at middle and high latitudes of the SH were faster and more stable than those in the NH. One reason is that the
501 SSW occurs frequently (6–7 times per decade) in the NH. During SSW, the eastward wind becomes weak or even reversal
502 (Butler et al., 2015; Baldwin et al., 2021). We note that SSWs in the NH mainly occurred in the phase when the zonal wind
503 was eastward (i.e., the zonal wind was eastward before and after SSWs, while the zonal wind becomes weak or reversed
504 during SSWs). In contrast, the SSW rarely occurred in the SH (only 3 time during 2002–2019, i.e., major SSW in September
505 2002, minor SSWs in August 2010 and September 2019), mainly due to the weaker land-sea contrast and smaller planetary
506 wave amplitudes in the SH than those in the NH (Eswaraiah et al., 2016; Li et al., 2021; Rao et al., 2020; Butler et al., 2015).

507 The MerU at 60°N/S and 30 km (Fig. 10) show that the SSWs in the NH have influence on the zonal wind at least in the
508 monthly mean sense. However, the influence of SSWs on the zonal wind in the SH is neglectable. If we simply use the zonal
509 wind at 60°N/S and 30 km as a predictor to represent SSW, the prominent responses appear in summer but not in winter
510 (when the SSW occur). This is because SSWs occur only in a limited temporal interval (1-2 weeks) in winter, the zonal wind
511 at 60°N/S and 30 km throughout the temporal interval include both SSWs and other variations. It is desired to develop an
512 index to represent the main features of SSW. This is out of the scope of this work and will be our future work. To illustrate
513 the possible influences of SSWs on BU, we show in Fig. 10 the residuals of BU (BU_{Res}) of Eq. (2) and their absolute values
514 ($|BU_{Res}|$) in a composite year. BU_{Res} may represent the effects SSWs on BU to some extent since we did not include SSW as
515 a regressor in Eq. (4).

516 From Fig. 10, we see that BU_{Res} have larger magnitudes (positive or negative) in the NH when SSWs occur. Meanwhile,
 517 the magnitudes of BU_{Res} decrease with the decreasing latitudes. $|BU_{Res}|$ in a composite year has peak around January, when
 518 SSWs occur more frequently as revealed from the MerU at 60°N . This indicates that the influences of SSWs on the
 519 regression results decrease with the decreasing latitudes in the NH. In contrast, BU_{Res} have larger magnitudes when the zonal
 520 winds decelerate from their eastward peaks in the SH. Further examination on the $|BU_{Res}|$ in a composite year, we see that
 521 their peaks shift from September at 50°S to July at lower latitudes. The larger $|BU_{Res}|$ in the SH is mainly due to the seasonal
 522 asymmetry of zonal winds, i.e., the zonal winds take a longer time to reach their eastward peak than that to reach their
 523 westward peak. The seasonal asymmetry of zonal winds might be induced by SAO and TAO.

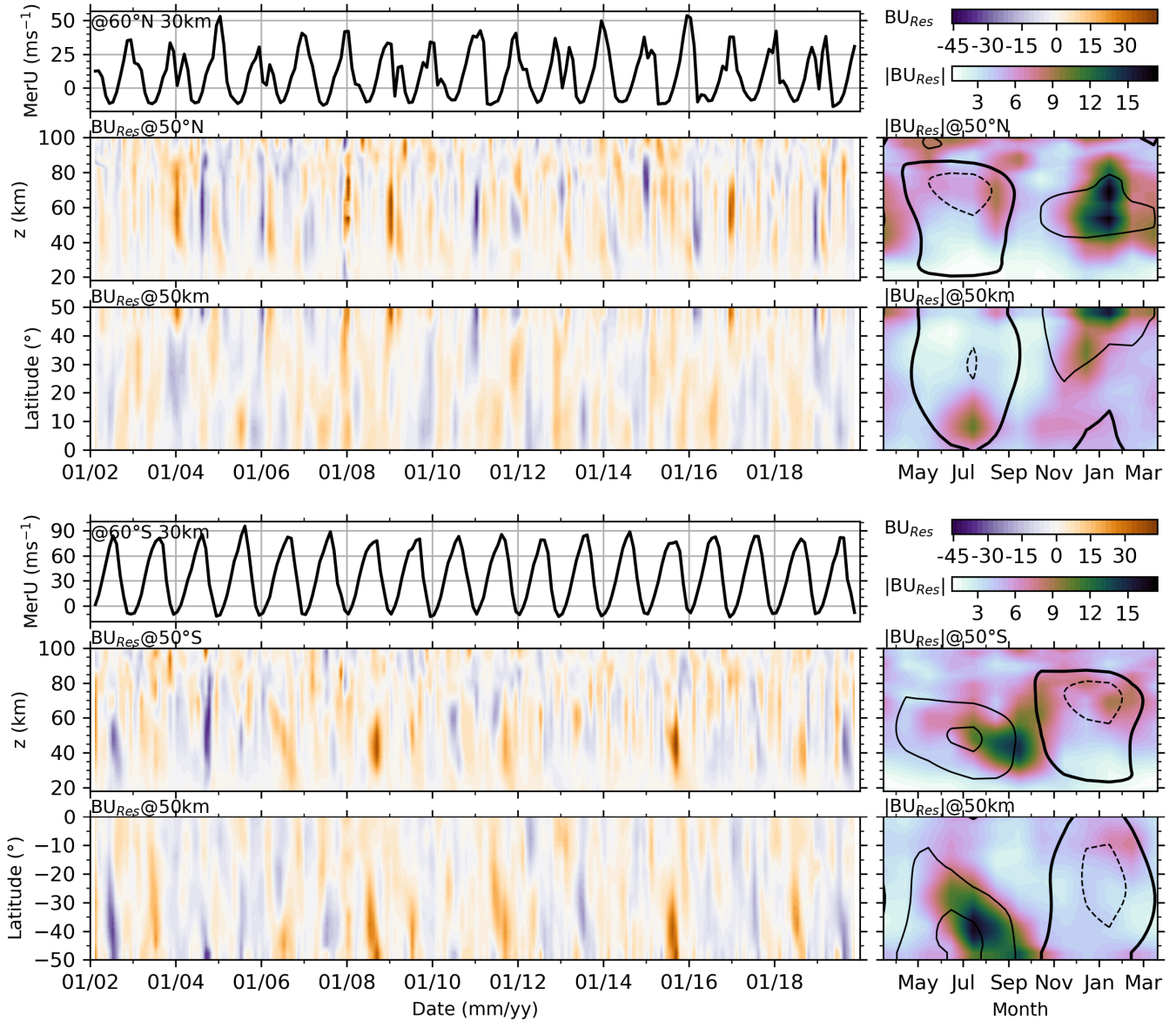


Figure 10: Upper three rows: MerU at 60°N and 30 km (first row) and the residuals of BU (BU_{res} , the upper color bar in the top-right corner) at 50°N (the second row) and 50 km (the third row), and the absolute values BU_{res} ($|BU_{res}|$, the lower color bar in the top-right corner) in a composite year. Lower three rows: same caption as the upper three rows but for the winds in the southern counterpart. The dashed, thick, and solid contour lines indicate the BU of -40, 0, 40 and 80 ms^{-1} , respectively.

524 To test the possible influences of SSWs on the hemispheric asymmetry of the variations and responses, we reconstruct
 525 the BU in the NH during 2002–2019 through the following two steps. First, at each height of the NH, we remove the wind
 526 data during SSWs (i.e., the BU in winter does not increase monotonically before December or decrease monotonically after

527 December, the specific years are 2003, 2004, 2006, 2007, 2008, 2009, 2013, 2018, 2019) from the raw wind (shown as black
528 dots in Fig. 11a). Second, cubic spline interpolation is applied on the remaining data (red dots in Fig. 11a) to get a
529 reconstructed wind series in winter (i.e., it increases monotonically before December and decreases monotonically after
530 December, shown as blue dashed line in Fig. 11a). Figures 11(b–d) show the raw BU, remaining and the reconstructed BU,
531 respectively. We see that the decelerated eastward winds during SSWs (Fig. 11b) have been replaced by the reconstructed
532 BU, i.e., the eastward winds accelerate before December and decelerate after December (Fig. 11d). According to $|BU_{Res}|$
533 shown in Fig. 10, we reconstruct the BU at 30°N – 50°N and throughout the height range.

534 Using the MLR procedure in Sec.2.2, we performed the same regression on the reconstructed winds in the NH. Figure
535 12 shows the amplitudes of seasonal variations and R^2 , and the responses of reconstructed winds to QBO, ENSO, F10.7, and
536 the linear variations. For comparison purpose, we also show in Fig. 12 the regression results of the raw BU. The R^2 indicates
537 that Eq. (2) explains the reconstructed winds similar to the raw BU in the NH stratospheric polar jet region. The amplitudes
538 of AO of the reconstructed winds are larger than those of the raw BU. However, the amplitudes of SAO and TAO of the
539 reconstructed winds are smaller than those of the raw BU in the NH stratospheric polar jet region. Above 80 km, the
540 amplitudes AO, SAO, TAO of both the reconstructed and raw BUs are nearly identical. This indicates that the influences of
541 SSWs on the seasonal variations mainly in the stratospheric polar jet region and around ~ 65 km.

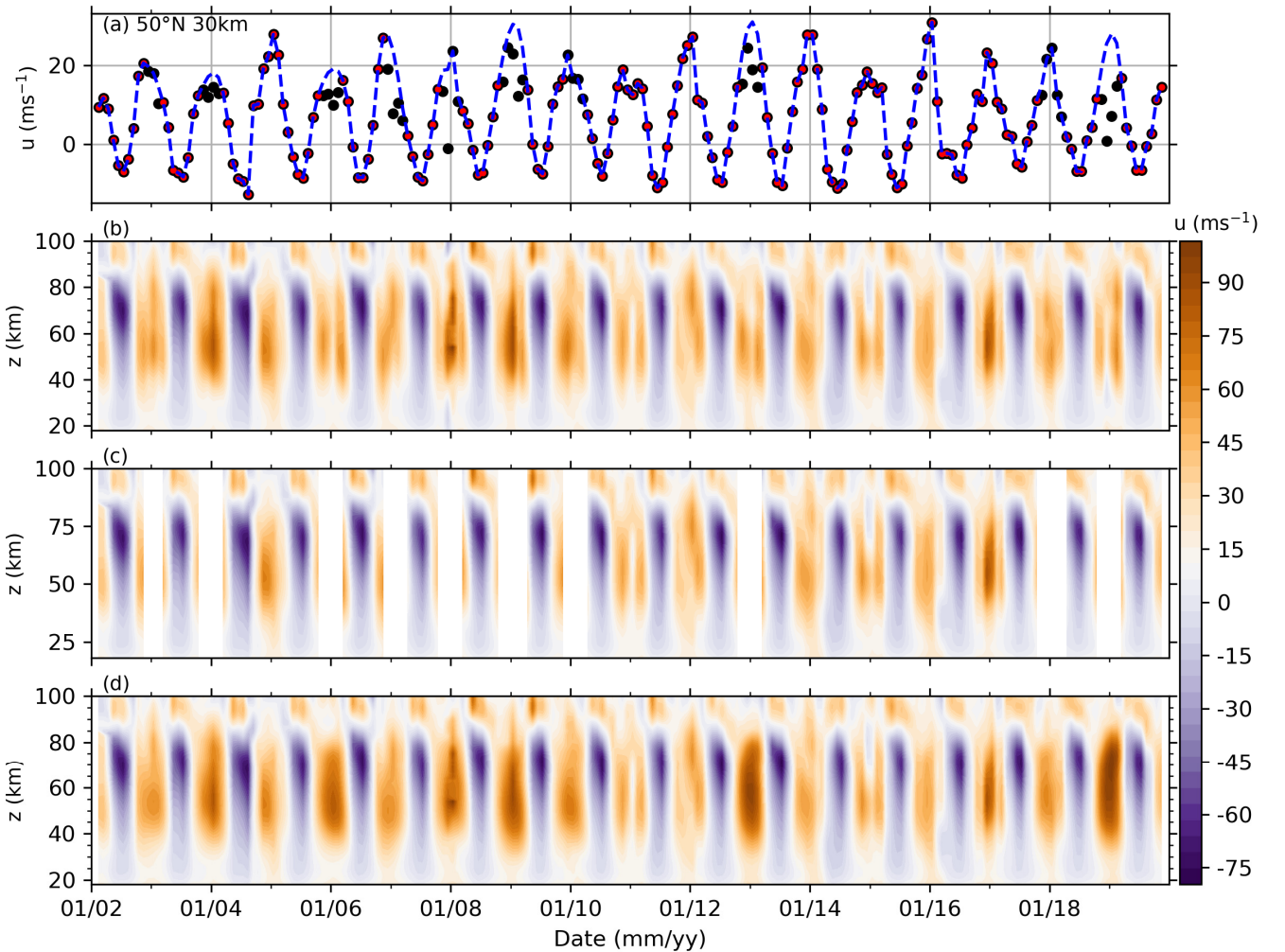


Figure 11: Removing SSWs from the raw BU and the reconstructed BU at 50°N . (a): the remaining data (red dots), which is obtained by removing the data affected by SSWs from raw BU (black dots), and the reconstructed BU (blue dotted line, see text for detail). (b–d): the raw BU, remaining and reconstructed BU, respectively.

542 In winter, the response of the reconstructed and raw BU to QBO_{30} and ENSO are similar on the aspects of both patterns

543 and magnitudes. However, at $\sim 30\text{--}60$ km and latitudes higher than 30°N , the responses of the reconstructed BU to F10.7 are
 544 more negative and significant. This is different from the positive and insignificant responses of the raw BU to F10.7 in the
 545 same region. The linear variations of the reconstructed BU are significant and extend to a wider latitude but at a lower height
 546 than those of the raw BU.

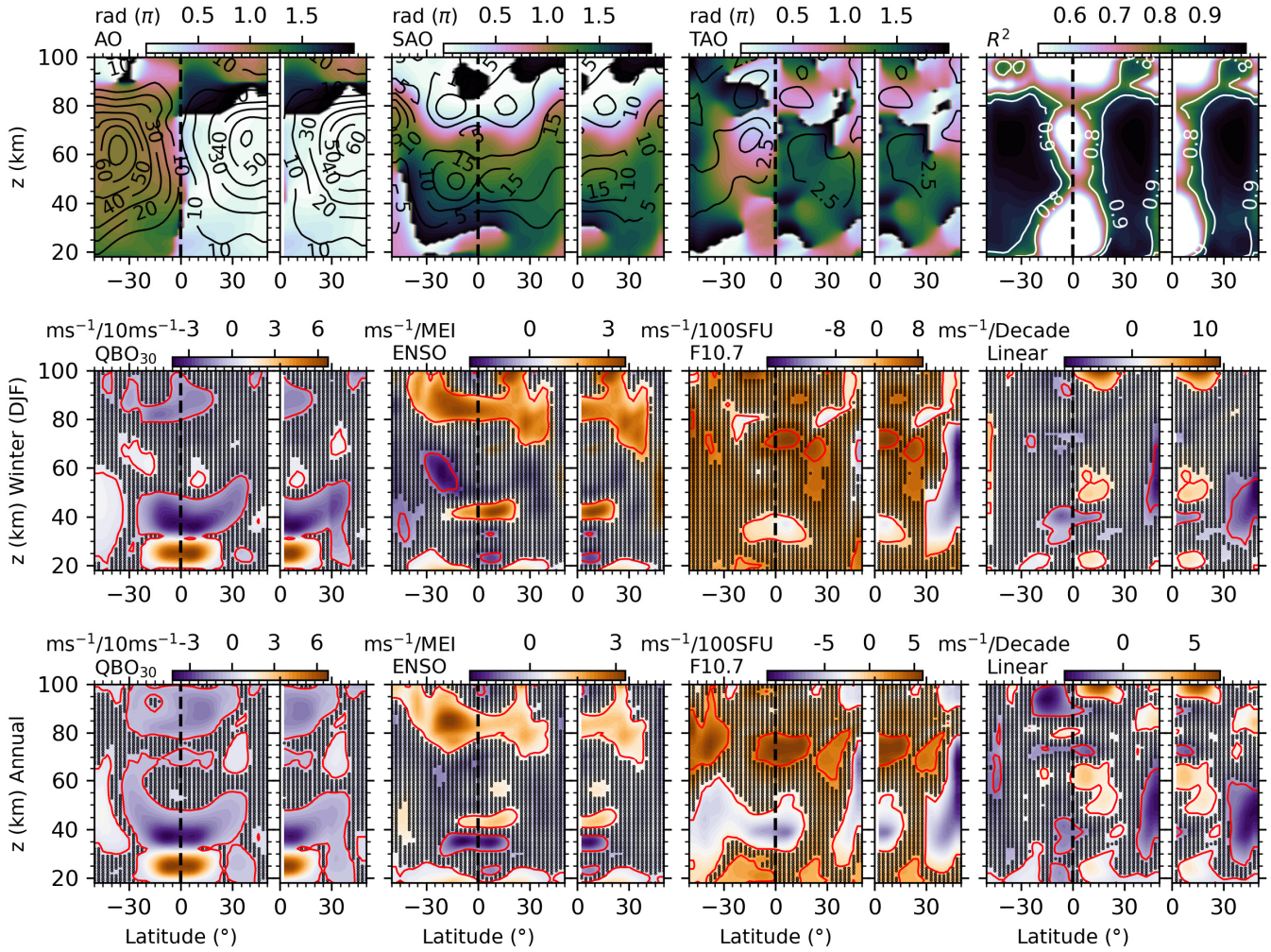


Figure 12: Regression results of the raw ($50^\circ\text{S}\text{--}50^\circ\text{N}$, left panel of each subplot) and reconstructed BU ($0^\circ\text{--}50^\circ\text{N}$, right panel of each subplot) in the NH during 2002–2019. Upper row: same caption as Fig. 3. Middle and lower row: same caption as Fig. 8 but for the responses of BU in winter (December-January-February) and in the annual mean, respectively.

547 The annual mean responses of the reconstructed and raw BU to QBO₃₀ and ENSO are similar on the aspects of both
 548 patterns and magnitudes. In contrast, at $\sim 30\text{--}60$ km and latitudes higher than 30°N , the annual mean responses of the
 549 reconstructed BU to F10.7 are negative and positive, which cover the entire NH as compared to the responses of the raw BU.
 550 The linear variations of the reconstructed winds are more negative at latitudes higher than 30°N at compared to linear
 551 variations of the raw BU.

552 In a word, compared to the raw BU, the reconstructed wind increases the amplitudes of AO but decreases the
 553 amplitudes of SAO and TAO in the NH stratospheric polar jet region. The responses of the reconstructed BU to QBO₃₀ and
 554 ENSO are similar to those of the raw BU on the aspects of both patterns and magnitudes and on the aspects of both winter
 555 and annual mean. However, at $\sim 30\text{--}60$ km and latitudes higher than 30°N , the responses of the reconstructed BU to F10.7
 556 and the linear variations of the reconstructed BU exhibit large differences as compared to the raw BU. However, the
 557 hemispheric asymmetry of the responses is not affected by SSWs at least in the monthly mean sense.

588 **5 Conclusions**

589 A global balance wind dataset (BU) is used to study the variations of the monthly zonal mean winds and the responses
590 of the monthly zonal mean winds to solar activity, QBO, ENSO at $\sim z=18\text{--}100$ km and $50^\circ\text{S}\text{--}50^\circ\text{N}$ and from 2002 to 2019.
591 The variations and responses are extracted by MLR method after removing the collinearity of predictors, which is also
592 applied to the MERRA2 zonal wind (MerU) to test the reliability of BU and their responses.

593 The seasonal variations (AO, SAO, and TAO) of BU and MerU have nearly identical phases. The consistencies of their
594 amplitudes are better in the SH than in the NH on the aspects of both patterns and magnitudes. The SAO of BU has peak
595 around 80 km is hemispheric asymmetry and stronger in the SH. The TAO of BU above 80 km is also hemispheric
596 asymmetry and stronger in the SH. The annual mean responses of BU and MerU to F10.7 are more negative in the SH
597 stratospheric polar jet region of SH than that of the NH counterpart. Around ~ 80 km, the annual responses of BU to F10.7
598 are mainly positive in the tropical region and high latitudes. The influences of the stratospheric QBO extend from the equator
599 to higher latitudes with the increasing height. The influences can be positive or negative, which depend on heights and
600 latitudes. Above ~ 80 km, the negative responses of winds to the stratospheric QBO are hemispheric asymmetry and are more
601 negative in the NH tropical regions. Both BU and MerU exhibit similar responses to MEI. Whereas the responses of BU to
602 MEI are stronger than those of MerU at 50°N/S . The responses of winds to MEI propagate downward with the increasing
603 time at 50°N/S and 25°N/S . Both BU and MerU exhibit similar linear variations. The large discrepancy is that the negative
604 variations of BU at 50°N cannot be seen in MerU during October–January. Above 70 km, the patterns of the linear variations
605 of BU are sporadic and strongly dependent on months, latitudes and heights.

606 The robustness of the responses of winds to QBO, ENSO, and F10.7, and the linear variations of winds are examined by
607 changing the temporal interval of the data. We found that the responses of winds to QBO are robust and are almost
608 independent on the temporal intervals. The responses of winds to ENSO are robust but slightly dependent on the temporal
609 intervals. Although the responses of wind to F10.7 have similar patterns in different temporal intervals, the responses are
610 stronger in the temporal intervals of 2002–2015 and 2002–2019 than the other two temporal intervals. The linear variations
611 of both BU and MerU depend strongly on the temporal intervals. The possible reasons might be the different linear
612 variations inhibited in the regressors and the unstable regressors in different temporal intervals. Thus, it is desired to examine
613 the responses and linear variations in different temporal intervals, such that one can get a more comprehensive impression on
614 the linear variations although the exact linear variations are unknown. The influences of SSWs on the seasonal variations are
615 mainly in the NH stratospheric polar jet region. However, the hemispheric asymmetry of the seasonal and linear variations,
616 and the hemispheric asymmetric responses of BU to QBO, ENSO, and F10.7 are not affected by SSWs at least in the
617 monthly mean sense.

588 **Data availability**

589 The global balance wind data can be obtained from National Space Science Data Center
590 (<https://doi.org/10.12176/01.99.00574>) (Last access: March 2022, Liu et al., 2021). The F10.7 data were obtained from
591 <https://spdf.gsfc.nasa.gov/pub/data/omni/> (last access: March 2022, Tapping, 2013). The MERRA2 data were obtained from
592 <http://disc.sci.gsfc.nasa.gov/mdisc> (last access: March 2022, Molod et al., 2015; Gelaro et al., 2017). The QBO data were
593 obtained from <https://www.geo.fu-berlin.de/en/met/ag/strat/produkte/qbo/> (last access: March 2022, Baldwin et al., 2001).
594 The ENSO data were obtained from <https://www.psl.noaa.gov/enso/mei/> (last access: March 2022, Zhang et al., 2019;
595 Wolter and Timlin, 2011).

596 **Author contributions**

597 XL analyzed the data and prepared the paper with assistance from co-authors. JX and JY design the study. All authors

598 reviewed and commented on the paper.

599 **Competing interests**

600 The authors declare that they have no conflict of interest.

601 **Acknowledgments**

602 This work was supported by the National Natural Science Foundation of China (41831073, 42174196, 41874182), the
603 Natural Science Foundation of Henan Province (212300410011), the Project of Stable Support for Youth Team in Basic
604 Research Field, CAS (YSBR-018), the Informatization Plan of Chinese Academy of Sciences (CAS-WX2021PY-0101), and
605 the Open Research Project of Large Research Infrastructures of CAS "Study on the interaction between low/mid-latitude
606 atmosphere and ionosphere based on the Chinese Meridian Project". This work was also supported in part by the Specialized
607 Research Fund and the Open Research Program of the State Key Laboratory of Space Weather.

608 **References**

- 609 Baldwin, M. P. and O'Sullivan, D.: Stratospheric Effects of ENSO-Related Tropospheric Circulation Anomalies, *J. Clim.*, 8,
610 649–667, [https://doi.org/10.1175/1520-0442\(1995\)008<0649:SEOERT>2.0.CO;2](https://doi.org/10.1175/1520-0442(1995)008<0649:SEOERT>2.0.CO;2), 1995.
- 611 Baldwin, M. P., Gray, L. J., Dunkerton, T. J., Hamilton, K., Haynes, P. H., Randel, W. J., Holton, J. R., Alexander, M. J.,
612 Hirota, I., Horinouchi, T., Jones, D. B. A., Kinnerson, J. S., Marquardt, C., Sato, K., and Takahashi, M.: The quasi-
613 biennial oscillation, *Rev. Geophys.*, 39, 179–229, <https://doi.org/10.1029/1999RG000073>, 2001.
- 614 Baldwin, M. P., Ayarzagüena, B., Birner, T., Butchart, N., Butler, A. H., Charlton-Perez, A. J., Domeisen, D. I. V., Garfinkel,
615 C. I., Garny, H., Gerber, E. P., Hegglin, M. I., Langematz, U., and Pedatella, N. M.: Sudden Stratospheric Warmings,
616 *Rev. Geophys.*, 59, <https://doi.org/10.1029/2020RG000708>, 2021.
- 617 Beig, G., Keckhut, P., Lowe, R. P., Roble, R. G., Mlynczak, M. G., Scheer, J., Fomichev, V. I., Offermann, D., French, W. J.
618 R., Shepherd, M. G., Semenov, A. I., Remsberg, E. E., She, C. Y., Lübken, F. J., Bremer, J., Clemesha, B. R., Stegman,
619 J., Sigernes, F., and Fadnavis, S.: Review of mesospheric temperature trends, *Rev. Geophys.*, 41,
620 <https://doi.org/10.1029/2002RG000121>, 2003.
- 621 Beig, G., Scheer, J., Mlynczak, M. G., and Keckhut, P.: Overview of the temperature response in the mesosphere and lower
622 thermosphere to solar activity, *Rev. Geophys.*, 46, <https://doi.org/10.1029/2007RG000236>, 2008.
- 623 Burrage, M. D., Vincent, R. A., Mayr, H. G., Skinner, W. R., Arnold, N. F., and Hays, P. B.: Long-term variability in the
624 equatorial middle atmosphere zonal wind, *J. Geophys. Res. Atmos.*, 101, 12847–12854,
625 <https://doi.org/10.1029/96JD00575>, 1996.
- 626 Butler, A. H., Seidel, D. J., Hardiman, S. C., Butchart, N., Birner, T., and Match, A.: Defining sudden stratospheric
627 warmings, *Bull. Am. Meteorol. Soc.*, 96, 1913–1928, <https://doi.org/10.1175/BAMS-D-13-00173.1>, 2015.
- 628 Cai, B., Xu, Q. C., Hu, X., Cheng, X., Yang, J. F., and Li, W.: Analysis of the correlation between horizontal wind and 11-
629 year solar activity over Langfang, China, *Earth Planet. Phys.*, 5, 270–279, <https://doi.org/10.26464/epp2021029>, 2021.
- 630 Coy, L., Wargan, K., Molod, A. M., McCarty, W. R., and Pawson, S.: Structure and dynamics of the quasi-biennial
631 oscillation in MERRA-2, *J. Clim.*, 29, 5339–5354, <https://doi.org/10.1175/JCLI-D-15-0809.1>, 2016.
- 632 Delisi, D. P. and Dunkerton, T. J.: Seasonal Variation of the Semiannual Oscillation, *J. Atmos. Sci.*, 45, 2772–2787,
633 [https://doi.org/10.1175/1520-0469\(1988\)045<2772:SVOTSO>2.0.CO;2](https://doi.org/10.1175/1520-0469(1988)045<2772:SVOTSO>2.0.CO;2), 1988.
- 634 Domeisen, D. I. V., Garfinkel, C. I., and Butler, A. H.: The teleconnection of El Niño Southern Oscillation to the
635 stratosphere, *Rev. Geophys.*, 57, 5–47, <https://doi.org/10.1029/2018RG000596>, 2019.
- 636 Dunkerton, T. J.: Theory of the Mesopause Semiannual Oscillation, *J. Atmos. Sci.*, 39, 2681–2690,
637 [https://doi.org/10.1175/1520-0469\(1982\)039<2681:TOTMSO>2.0.CO;2](https://doi.org/10.1175/1520-0469(1982)039<2681:TOTMSO>2.0.CO;2), 1982.
- 638 Emmert, J. T., Stevens, M. H., Bernath, P. F., Drob, D. P., and Boone, C. D.: Observations of increasing carbon dioxide
639 concentration in Earth's thermosphere, *Nat. Geosci.*, 5, 868–871, <https://doi.org/10.1038/ngeo1626>, 2012.
- 640 Ern, M., Diallo, M., Preusse, P., Mlynczak, M. G., Schwartz, M. J., Wu, Q., and Riese, M.: The semiannual oscillation (SAO)
641 in the tropical middle atmosphere and its gravity wave driving in reanalyses and satellite observations, *Atmos. Chem.*
642 *Phys.*, 21, 13763–13795, <https://doi.org/10.5194/acp-21-13763-2021>, 2021.
- 643 Eswaraiyah, S., Kim, Y. H., Hong, J., Kim, J. H., Ratnam, M. V., Chandran, A., Rao, S. V. B., and Riggan, D.: Mesospheric
644 signatures observed during 2010 minor stratospheric warming at King Sejong Station (62°S, 59°W), *J. Atmos. Solar-*
645 *Terrestrial Phys.*, 140, 55–64, <https://doi.org/10.1016/j.jastp.2016.02.007>, 2016.
- 646 Fleming, E. L., Chandra, S., Barnett, J. J., and Corney, M.: Zonal mean temperature, pressure, zonal wind and geopotential
647 height as functions of latitude, *Adv. Sp. Res.*, 10, 11–59, [https://doi.org/10.1016/0273-1177\(90\)90386-E](https://doi.org/10.1016/0273-1177(90)90386-E), 1990.
- 648 Garcia, R. R., Dunkerton, T. J., Lieberman, R. S., and Vincent, R. A.: Climatology of the semiannual oscillation of the
649 tropical middle atmosphere, *J. Geophys. Res. Atmos.*, 102, <https://doi.org/10.1029/97jd00207>, 1997.

650 Garcia, R. R., Yue, J., and Russell, J. M.: Middle atmosphere temperature trends in the twentieth and twenty-first centuries
651 simulated with the Whole Atmosphere Community Climate Model (WACCM), *J. Geophys. Res. Sp. Phys.*, 124, 7984–
652 7993, <https://doi.org/10.1029/2019JA026909>, 2019.

653 Gelaro, R., McCarty, W., Suárez, M. J., Todling, R., Molod, A., Takacs, L., Randles, C. A., Darmenov, A., Bosilovich, M.
654 G., Reichle, R., Wargan, K., Coy, L., Cullather, R., Draper, C., Akella, S., Buchard, V., Conaty, A., da Silva, A. M., Gu,
655 W., Kim, G. K., Koster, R., Lucchesi, R., Merkova, D., Nielsen, J. E., Partyka, G., Pawson, S., Putman, W., Rienecker,
656 M., Schubert, S. D., Sienkiewicz, M., and Zhao, B.: The modern-era retrospective analysis for research and applications,
657 version 2 (MERRA-2), *J. Clim.*, 30, 5419–5454, <https://doi.org/10.1175/JCLI-D-16-0758.1>, 2017.

658 Hayashi, H., Koyama, Y., Hori, T., Tanaka, Y., Abe, S., Shinbori, A., Kagitani, M., Kouno, T., Yoshida, D., UeNo, S.,
659 Kaneda, N., Yoneda, M., Umemura, N., Tadokoro, H., and Motoba, T.: Inter-university upper atmosphere global
660 observation network (IUGONET), *Data Sci. J.*, 12, 179–184, <https://doi.org/10.2481/dsj.WDS-030>, 2013.

661 Hitchman, M. H. and Leovy, C. B.: Evolution of the Zonal Mean State in the Equatorial Middle Atmosphere during October
662 1978–May 1979, *J. Atmos. Sci.*, 43, 3159–3176, [https://doi.org/10.1175/1520-469\(1986\)043<3159:EOTZMS>2.0.CO;2](https://doi.org/10.1175/1520-469(1986)043<3159:EOTZMS>2.0.CO;2), 1986.

663 Keuer, D., Hoffmann, P., Singer, W., and Bremer, J.: Long-term variations of the mesospheric wind field at mid-latitudes,
664 *Ann. Geophys.*, 25, 1779–1790, <https://doi.org/10.5194/angeo-25-1779-2007>, 2007.

665 Kumar, K. K.: Is Mesospheric Quasi Biennial Oscillation Ephemeral?, *Geophys. Res. Lett.*, 48,
666 <https://doi.org/10.1029/2020GL091033>, 2021.

667 Kutner, M., Neter, C. N. J., and Li, W.: *Applied Linear Statistical Models*, 5th ed., McGraw-Hill Irwin, Boston, 258 pp.,
668 2004.

669 Laštovička, J.: A review of recent progress in trends in the upper atmosphere, *J Atmos Sol Terr Phys*, 163, 2–13,
670 <https://doi.org/10.1016/j.jastp.2017.03.009>, 2017.

671 Li, N., Lei, J., Huang, F., Yi, W., Chen, J., Xue, X., Gu, S., Luan, X., Zhong, J., Liu, F., Dou, X., Qin, Y., and Owolabi, C.:
672 Responses of the ionosphere and neutral winds in the mesosphere and lower thermosphere in the Asian-Australian
673 sector to the 2019 Southern Hemisphere Sudden Stratospheric Warming, *J. Geophys. Res. Sp. Phys.*, 126,
674 <https://doi.org/10.1029/2020JA028653>, 2021.

675 Li, T., Calvo, N., Yue, J., Dou, X., Russell, J. M., Mlynczak, M. G., She, C. Y., and Xue, X.: Influence of El Niño-Southern
676 oscillation in the mesosphere, *Geophys. Res. Lett.*, 40, 3292–3296, <https://doi.org/10.1002/grl.50598>, 2013.

677 Li, T., Calvo, N., Yue, J., Russell, J. M., Smith, A. K., Mlynczak, M. G., Chandran, A., Dou, X., and Liu, A. Z.: Southern
678 Hemisphere summer mesopause responses to El Niño-Southern Oscillation, *J. Clim.*, 29, 6319–6328,
679 <https://doi.org/10.1175/JCLI-D-15-0816.1>, 2016.

680 Li, T., Leblanc, T., McDermid, I. S., Keckhut, P., Hauchecorne, A., and Dou, X.: Middle atmosphere temperature trend and
681 solar cycle revealed by long-term Rayleigh lidar observations, *Journal of Geophysical Research Atmospheres*, 116, 1–
682 11, <https://doi.org/10.1029/2010JD015275>, 2011.

683 Li, T., Liu, A. Z., Lu, X., Li, Z., Franke, S. J., Swenson, G. R., and Dou, X.: Meteor-radar observed mesospheric semi-
684 annual oscillation (SAO) and quasi-biennial oscillation (QBO) over Maui, Hawaii, *J. Geophys. Res. Atmos.*, 117,
685 <https://doi.org/10.1029/2011JD016123>, 2012.

686 Lin, J. and Qian, T.: Impacts of the ENSO lifecycle on stratospheric ozone and temperature, *Geophys Res Lett*, 46, 10646–
687 10658, <https://doi.org/10.1029/2019GL083697>, 2019.

688 Liu, X., Yue, J., Xu, J., Garcia, R. R., Russell, J. M., Mlynczak, M., Wu, D. L., and Nakamura, T.: Variations of global
689 gravity waves derived from 14 years of SABER temperature observations, *J. Geophys. Res. Atmos.*, 122, 6231–6249,
690 <https://doi.org/10.1002/2017JD026604>, 2017.

691 Liu, X., Xu, J., Yue, J., Yu, Y., Batista, P. P., Andrioli, V. F., Liu, Z., Yuan, T., Wang, C., Zou, Z., Li, G., and Russell III, J.
692 M.: Global balanced wind derived from SABER temperature and pressure observations and its validations, *Earth Syst.*
693 *Sci. Data*, 13, 5643–5661, <https://doi.org/10.5194/essd-13-5643-2021>, 2021.

694 Liu, X., Xu, J., Yue, J., and Kogure, M.: Persistent layers of enhanced gravity wave dissipation in the upper mesosphere
695 revealed from SABER observations, *Geophys. Res. Lett.*, 49, 1–11, <https://doi.org/10.1029/2021GL097038>, 2022.

696 Lübken, F. J., Baumgarten, G., Fiedler, J., Gerding, M., Höffner, J., and Berger, U.: Seasonal and latitudinal variation of
697 noctilucent cloud altitudes, *Geophys. Res. Lett.*, 35, 1–4, <https://doi.org/10.1029/2007GL032281>, 2008.

698 Manney, G. L. and Hegglin, M. I.: Seasonal and regional variations of long-term changes in upper-tropospheric jets from
699 reanalyses, *J. Clim.*, 31, 423–448, <https://doi.org/10.1175/JCLI-D-17-0303.1>, 2018.

700 Manzini, E., Giorgetta, M. A., Esch, M., Kornblueh, L., and Roeckner, E.: The influence of sea surface temperatures on the
701 northern winter stratosphere: ensemble simulations with the MAECHAM5 model, *J. Clim.*, 19, 3863–3881,
702 <https://doi.org/10.1175/JCLI3826.1>, 2006.

703 Matsumoto, N., Shinbori, A., Riggan, D. M., and Tsuda, T.: Measurement of momentum flux using two meteor radars in
704 Indonesia, *Ann. Geophys.*, 34, 369–377, <https://doi.org/10.5194/angeo-34-369-2016>, 2016.

705 Mitchell, D. M., Gray, L. J., Fujiwara, M., Hibino, T., Anstey, J. A., Ebisuzaki, W., Harada, Y., Long, C., Misios, S., Stott, P.
706 A., and Tan, D.: Signatures of naturally induced variability in the atmosphere using multiple reanalysis datasets, *Q. J. R.*
707 *Meteorol. Soc.*, 141, 2011–2031, <https://doi.org/10.1002/qj.2492>, 2015.

708 Mlynczak, M. G., Hunt, L. A., Garcia, R. R., Harvey, V. L., Marshall, B. T., Yue, J., Mertens, C. J., and Russell, J. M.:
709 Cooling and Contraction of the Mesosphere and Lower Thermosphere From 2002 to 2021, *Journal of Geophysical*
710 *Research: Atmospheres*, 127, <https://doi.org/10.1029/2022JD036767>, 2022.

712 Molod, A., Takacs, L., Suarez, M., and Bacmeister, J.: Development of the GEOS-5 atmospheric general circulation model:
713 evolution from MERRA to MERRA2, *Geosci. Model Dev.*, 8, 1339–1356, <https://doi.org/10.5194/gmd-8-1339-2015>,
714 2015.

715 Mudelsee, M.: Trend analysis of climate time series: A review of methods, *Earth-Science Rev.*, 190, 310–322,
716 <https://doi.org/10.1016/j.earscirev.2018.12.005>, 2019.

717 Pukite, P., Coyne, D., and Challou, D.: *Mathematical Geoenery*, Wiley, <https://doi.org/10.1002/9781119434351>, 2018.

718 Polvani, L. M. and Waugh, D. W.: Upward wave activity flux as a precursor to extreme stratospheric events and subsequent
719 anomalous surface weather regimes, *J. Clim.*, 17, 3548–3554, [https://doi.org/10.1175/1520-0442\(2004\)017<3548:UWAFAA>2.0.CO;2](https://doi.org/10.1175/1520-0442(2004)017<3548:UWAFAA>2.0.CO;2), 2004.

720 Qian, L., Jacobi, C., and McInerney, J.: Trends and Solar Irradiance Effects in the Mesosphere, *J Geophys Res Space Phys*,
721 124, 1343–1360, <https://doi.org/10.1029/2018JA026367>, 2019.

722 Ramesh, K., Smith, A. K., Garcia, R. R., Marsh, D. R., Sridharan, S., and Kishore Kumar, K.: Long-term variability and
723 tendencies in middle atmosphere temperature and zonal wind from WACCM6 simulations during 1850–2014, *J.*
724 *Geophys. Res. Atmos.*, 125, <https://doi.org/10.1029/2020JD033579>, 2020.

725 Randel, W. J.: The Evaluation of Winds from geopotential height data in the stratosphere, *J. Atmos. Sci.*, 44, 3097–3120,
726 [https://doi.org/10.1175/1520-0469\(1987\)044<3097:TEOWFG>2.0.CO;2](https://doi.org/10.1175/1520-0469(1987)044<3097:TEOWFG>2.0.CO;2), 1987.

727 Randel, W. J. and Cobb, J. B.: Coherent variations of monthly mean total ozone and lower stratospheric temperature, *J*
728 *Geophys Res*, 99, 5433, <https://doi.org/10.1029/93JD03454>, 1994.

729 Randel, W. J., Garcia, R. R., Calvo, N., and Marsh, D.: ENSO influence on zonal mean temperature and ozone in the tropical
730 lower stratosphere, *Geophys. Res. Lett.*, 36, <https://doi.org/10.1029/2009GL039343>, 2009.

731 Randel, W. J., Polvani, L., Wu, F., Kinnison, D. E., Zou, C. Z., and Mears, C.: Troposphere-stratosphere temperature trends
732 derived from satellite data compared with ensemble simulations from WACCM, *J. Geophys. Res. Atmos.*, 122, 9651–
733 9667, <https://doi.org/10.1002/2017JD027158>, 2017.

734 Randel, W. J., Udelhofen, P., Fleming, E., Geller, M., Gelman, M., Hamilton, K., Karoly, D., Ortland, D., Pawson, S.,
735 Swinbank, R., Wu, F., Baldwin, M., Chanin, M.-L., Keckhut, P., Labitzke, K., Remsberg, E., Simmons, A., and Wu, D.:
736 The SPARC intercomparison of middle-atmosphere climatologies, *J. Clim.*, 17, 986–1003,
737 [https://doi.org/10.1175/1520-0442\(2004\)017<0986:TSIOMC>2.0.CO;2](https://doi.org/10.1175/1520-0442(2004)017<0986:TSIOMC>2.0.CO;2), 2004.

738 Rao, J., Garfinkel, C. I., White, I. P., and Schwartz, C.: The southern hemisphere minor sudden stratospheric warming in
739 September 2019 and its predictions in S2S models, *J. Geophys. Res. Atmos.*, 125,
740 <https://doi.org/10.1029/2020JD032723>, 2020.

741 Ray, E. A., Alexander, M. J., and Holton, J. R.: An analysis of the structure and forcing of the equatorial semiannual
742 oscillation in zonal wind, *J. Geophys. Res. Atmos.*, 103, 1759–1774, <https://doi.org/10.1029/97JD02679>, 1998.

743 Russell III, J. M., Mlynczak, M. G., Gordley, L. L., Tansock, Jr., J. J., and Esplin, R. W.: Overview of the SABER
744 experiment and preliminary calibration results, in: *Optical Spectroscopic Techniques and Instrumentation for*
745 *Atmospheric and Space Research III*, 277–288, <https://doi.org/10.1117/12.366382>, 1999.

746 She, C., Berger, U., Yan, Z., Yuan, T., Lübken, F. -J., Krueger, D. A., and Hu, X.: Solar response and long-term trend of
747 midlatitude mesopause region temperature based on 28 Years (1990–2017) of Na lidar observations, *J. Geophys. Res.*
748 *Sp. Phys.*, 124, 7140 – 7156, <https://doi.org/10.1029/2019JA026759>, 2019.

749 Smith, A. K., Garcia, R. R., Moss, A. C., and Mitchell, N. J.: The semiannual oscillation of the tropical zonal wind in the
750 middle atmosphere derived from satellite geopotential height retrievals, *J. Atmos. Sci.*, 74, 2413–2425,
751 <https://doi.org/10.1175/JAS-D-17-0067.1>, 2017.

752 Souleymane, S., Madonna, F., Rosoldi, M., Tramutola, E., Gagliardi, S., Proto, M., and Pappalardo, G.: Sensitivity of trends
753 to estimation methods and quantification of subsampling effects in global radiosounding temperature and humidity time
754 series, *Int. J. Climatol.*, 41, E1992–E2014, <https://doi.org/10.1002/joc.6827>, 2021.

755 Sridharan, S., Tsuda, T., and Gurubaran, S.: Radar observations of long-term variability of mesosphere and lower
756 thermosphere winds over Tirunelveli (8.7°N, 77.8°E), *J. Geophys. Res. Atmos.*, 112,
757 <https://doi.org/10.1029/2007JD008669>, 2007.

758 Swinbank, R. and Ortland, D. A.: Compilation of wind data for the Upper Atmosphere Research Satellite (UARS) Reference
759 Atmosphere Project, *J. Geophys. Res.*, 108, 4615, <https://doi.org/10.1029/2002jd003135>, 2003.

760 Taguchi, M.: Observed connection of the stratospheric quasi-biennial oscillation with El Niño–Southern Oscillation in
761 radiosonde data, *J. Geophys. Res.*, 115, D18120, <https://doi.org/10.1029/2010JD014325>, 2010.

762 Tapping, K. F.: The 10.7 cm solar radio flux (F10.7), *Sp. Weather*, 11, 394–406, <https://doi.org/10.1002/swe.20064>, 2013.

763 Venkat Ratnam, M., Kishore Kumar, G., Venkateswara Rao, N., Krishna Murthy, B. V., Laštovička, J., and Qian, L.:
764 Evidence of long-term change in zonal wind in the tropical lower mesosphere: Observations and model simulations,
765 *Geophys. Res. Lett.*, 40, 397–401, <https://doi.org/10.1002/grl.50158>, 2013.

766 Venkat Ratnam, M., Akhil Raj, S. T., and Qian, L.: Long-term trends in the low-latitude middle atmosphere temperature and
767 winds: observations and WACCM-X model simulations, *J. Geophys. Res. Sp. Phys.*, 124, 7320–7331,
768 <https://doi.org/10.1029/2019JA026928>, 2019.

769 Venkateswara Rao, N., Tsuda, T., Riggan, D. M., Gurubaran, S., Reid, I. M., and Vincent, R. A.: Long-term variability of
770 mean winds in the mesosphere and lower thermosphere at low latitudes, *J Geophys. Res. Sp. Phys.*, 117, 1–16,
771 <https://doi.org/10.1029/2012JA017850>, 2012.

772 Wolter, K. and Timlin, M. S.: El Niño/Southern Oscillation behaviour since 1871 as diagnosed in an extended multivariate
773 ENSO index (MEI.ext), *Int. J. Climatol.*, 31, 1074–1087, <https://doi.org/10.1002/joc.2336>, 2011.

774

775 Xu, J., Liu, H.-L., Yuan, W., Smith, A. K., Roble, R. G., Mertens, C. J., Russell, J. M., and Mlynczak, M. G.: Mesopause
776 structure from Thermosphere, Ionosphere, Mesosphere, Energetics, and Dynamics (TIMED)/Sounding of the
777 Atmosphere Using Broadband Emission Radiometry (SABER) observations, *J. Geophys. Res.*, 112, D09102,
778 <https://doi.org/10.1029/2006JD007711>, 2007.

779 Xu, J., Smith, A. K., Liu, H.-L., Yuan, W., Wu, Q., Jiang, G., Mlynczak, M. G., and Russell, J. M.: Estimation of the
780 equivalent Rayleigh friction in mesosphere/lower thermosphere region from the migrating diurnal tides observed by
781 TIMED, *J. Geophys. Res.*, 114, D23103, <https://doi.org/10.1029/2009JD012209>, 2009a.

782 Xu, J., Smith, A. K., Liu, H. L., Yuan, W., Wu, Q., Jiang, G., Mlynczak, M. G., Russell, J. M., and Franke, S. J.: Seasonal
783 and quasi-biennial variations in the migrating diurnal tide observed by Thermosphere, Ionosphere, Mesosphere,
784 Energetics and Dynamics (TIMED), *J. Geophys. Res. Atmos.*, 114, 1–16, <https://doi.org/10.1029/2008jd011298>, 2009b.

785 Yuan, T., Solomon, S. C., She, C. -Y., Krueger, D. A., and Liu, H. -L.: The long-term trends of nocturnal mesopause
786 temperature and altitude revealed by Na lidar observations between 1990 and 2018 at Midlatitude, *J. Geophys. Res.*
787 *Atmos.*, 124, 5970–5980, <https://doi.org/10.1029/2018JD029828>, 2019.

788 Yue, J., Russell, J., Jian, Y., Rezac, L., Garcia, R., López-Puertas, M., and Mlynczak, M. G.: Increasing carbon dioxide
789 concentration in the upper atmosphere observed by SABER, *Geophys. Res. Lett.*, 42, 7194–7199,
790 <https://doi.org/10.1002/2015GL064696>, 2015.

791 Yue, J., Russell, J., Gan, Q., Wang, T., Rong, P., Garcia, R., and Mlynczak, M.: Increasing water vapor in the stratosphere
792 and mesosphere after 2002, *Geophys. Res. Lett.*, 46, 13452–13460, <https://doi.org/10.1029/2019GL084973>, 2019a.

793 Yue, J., Li, T., Qian, L., Lastovicka, J., and Zhang, S.: Introduction to special issue on “long-term changes and trends in the
794 middle and upper atmosphere,” *J. Geophys. Res. Sp. Phys.*, 124, 10360–10364, <https://doi.org/10.1029/2019JA027462>,
795 2019b.

796 Zhang, S., Cnossen, I., Laštovička, J., Elias, A. G., Yue, X., Jacobi, C., Yue, J., Wang, W., Qian, L., and Goncharenko, L.:
797 Long-term geospace climate monitoring, *Front. Astron. Sp. Sci.*, 10, 1–5, <https://doi.org/10.3389/fspas.2023.1139230>,
798 2023.

799 Zhang, T., Hoell, A., Perlwitz, J., Eischeid, J., Murray, D., Hoerling, M., and Hamill, T. M.: Towards probabilistic
800 multivariate ENSO monitoring, *Geophys. Res. Lett.*, 46, 10532–10540, <https://doi.org/10.1029/2019GL083946>, 2019.

801